ELSEVIER

Contents lists available at ScienceDirect

#### International Journal of Biological Macromolecules

journal homepage: www.elsevier.com/locate/ijbiomac



## Xanthan-based nanocomplexes: modulating colloidal properties, model compound encapsulation and mucoadhesion via diethylaminoethyl dextran

Ioannis Pispas <sup>a,b</sup>, Ewa Pavlova <sup>c</sup>, Miroslav Slouf <sup>c</sup>, Aristeidis Papagiannopoulos <sup>a,\*</sup>

- a Theoretical and Physical Chemistry Institute, National Hellenic Research Foundation, 48 Vassileos Constantinou Avenue, 11635, Athens, Greece
- b Department of Physics, School of Applied Mathematical and Physical Sciences, National Technical University of Athens, Heroon Polytechniou 9, Zografou, 15780, Athens Greece
- <sup>c</sup> Institute of Macromolecular Chemistry, Czech Academy of Sciences, Heyrovského nám. 2, 162 06, Prague 6, Czech Republic

#### ARTICLE INFO

# Keywords: Polysaccharide nanoparticles Polysaccharide nanogels Mucus analogs Mucus mimics β-Carotene

#### ABSTRACT

Xanthan gum (XG) and diethylaminoethyl dextran (DD) electrostatic nanocomplexes (NCs) are prepared at the native (NCs) and thermally denatured state of XG (den-NCs). Dynamic and static light scattering (DLS and SLS) and transmission electron microscopy (TEM) reveal well-defined, spherical NCs with mean hydrodynamic and gyroscopic radii of 100–200 nm at charge ratios (ratio of anionic XG to cationic DD monomers) between 0.4 and 5. Their size increases at CR > 1 possibly due to XG-XG double helix formation. Surface potential shifts from positive to negative between CR 1 and 1.25, suggesting stoichiometric neutralization. NCs remain stable for over one month without significant aggregation. Fluorescence measurements with pyrene and 8-Anilino-1-naphthalenesulfonate (ANS) indicate the presence of hydrophobic domains inside the NCs attributed to DD's ethyl groups, which renders them suitable for the encapsulation of hydrophobic compounds. High loading efficiency ( $\sim$ 48 %) and loading capacity ( $\sim$ 19 %) for  $\beta$ -carotene ( $\beta$ -C) is found for native NCs at CR 0.4 and 2.5, whereas den-NCs show significantly lower encapsulation. NCs interact with porcine gastric mucin (PGM) in PGM solutions as it is confirmed by NC-PGM aggregation. Mucoadhesion is also examined with mucus-mimicking PGM-immobilized alginate beads. Positively charged NCs exhibit enhanced mucoadhesion relative to negatively charged ones. Overall, XG/DD NCs display tunable properties promising for drug delivery applications with notable stability, encapsulation and mucoadhesive capabilities.

#### 1. Introduction

Electrostatically assembled nanoparticles formed by combining anionic and cationic polysaccharides have gathered significant attention due to their potential applications in the nanodelivery of drugs [1] and food substances [2]. Polysaccharide nanoassemblies leverage the natural biocompatibility, biodegradability, and functional versatility of polysaccharides and therefore attract interest for the creation of nanoscale carriers capable of encapsulating active compounds [3]. In drug delivery, they have been employed to enhance the solubility, stability, and controlled release of therapeutic agents, thereby improving their bioavailability and reducing side effects [4–9]. In the food science, they have been utilized to encapsulate and protect sensitive nutrients, flavors, and bioactive compounds, ensuring their stability during processing and enhancing their bioavailability upon consumption [4,10,11]. The physical process of polyelectrolyte complexation [12]

involves electrostatic interactions between oppositely charged macromolecules. This spontaneous formation of nanostructures without the need of any chemical reactions opens opportunities for green methodologies based on synthetic and natural polyelectrolytes [13–15].

Xanthan gum (XG) is a semiflexible polysaccharide of high molar mass ( $\sim 2 \cdot 10^6 \text{ gmol}^{-1} \text{ [16,17]}$ ) originating by fermentation from *Xanthomonas campestris* [18]. It is an anionic polyelectrolyte with trisaccharide side-chains and with chargeable mannose groups, grafted on a backbone of cellulose [19,20]. It is known that in natural XG produced by *Xanthomonas campestris*  $\sim 90$  % of the internal mannose units of the side chains are acetylated and 30–50 % of the terminal mannose residues are pyruvated [21]. In aqueous media it forms self-similar viscoelastic fluids [22,23] and it can transform into colloidal liquids with modifiable properties upon interaction with charged substances such as cationic surfactants [24], proteins [25,26] and cationic polysaccharides [27]. It has been used in nanodelivery of therapeutic agents

E-mail address: apapagiannopoulos@eie.gr (A. Papagiannopoulos).

<sup>\*</sup> Corresponding author.

[28] and in food industry as an excellent viscosity modifier [19]. It exhibits mucoadhesive properties and therefore has been used in various applications e.g., as an excipient for controlled-release in buccal films [29,30], in nicotine mucoadhesive patches [31] and in hydrogels for local release of anti-Candida peptide [32]. Diethylaminoethyl dextran (DD) is a cationic polysaccharide consisting of three amino groups on its monomeric unit, namely two tertiary groups with pKa of 9.5 and 5.7 and a quaternary group with pKa of 14 [33,34]. Similarly to XG, it has been proposed for drug delivery [33,35,36] and m-RNA encapsulation [37]. The cationic polysaccharide DD is anticipated to lead to the formation of nanocomplexes (NCs) with XG. DD has the potential to modify the drug encapsulation and delivery properties of the XG-based NCs due to presence of hydrophobic ethyl groups on its side-chains [33,36,38] and its ability to act as a therapeutic agent on its own [39].

In this work, electrostatic NCs of XG and DD were developed across a wide range of XG-to-DD charge ratios (CRs) to assess whether the colloidal properties, encapsulation efficiency, and mucoadhesive capabilities of XG can be systematically tuned by DD. Light scattering and transmission electron microscopy methods were applied for the characterization of the mass, size distribution, morphology, surface charge and stability of the NCs. The interactions of the NCs with the model hydrophobic molecules pyrene and ANS at different CRs were investigated by fluorescence spectroscopy. The encapsulation of  $\beta$ -carotene by the NCs was quantified by UV-Visible spectroscopy. These physicochemical experimental techniques gave insight into the relationship between the distribution of XG and DD chain segments in the NCs at different CRs with their ability to encapsulate hydrophobic substances. To understand and potentially predict the interactions of NCs with mucus at a molecular level, we conducted experiments where NCs interacted with porcine gastric mucin (PGM) alone and immobilized PGM on alginate beads. This work demonstrates how a systematic approach to the electrostatic assembly of polysaccharide nanocomplexes can be applied to design and optimize their colloidal properties and molecular interactions with molecular compounds and biological systems, providing a framework for developing tailored delivery systems for pharmaceutical and food applications.

#### 2. Materials and methods

#### 2.1. Materials and sample preparation

#### 2.1.1. Materials

Xanthan gum (XG) was purchased from CP Kelco. Diethylaminoethyl-dextran (DD) with molar mass  $1.50 \cdot 10^5 \text{ gmol}^{-1}$ , pyrene, 8-Anilino-1-naphthalenesulfonate (ANS),  $\beta$ -carotene ( $\beta$ -C), mucin from porcine stomach (Type III) (PGM) and alginic acid sodium salt from brown algae (low viscosity) (ALG) were purchased from Sigma Aldrich.

#### 2.1.2. Preparation of NCs

The preparation of the NCs was based on the methodology of our previous works on polysaccharide/protein complexes [40,41]. All stock solutions were prepared under stirring at pH 7 using sterile, non-pyrogenic water for injection (to eliminate the growth of bacteria) as the solvent. The stock solutions of XG and DD were prepared at 1 mg/mL and kept for one day at 4 °C to attain equilibrium. Charge ratios CR = [-]/[+] of XG to DD at 0.1, 0.2, 0.4, 0.8, 1, 1.25, 2.5, 5 and 10 were used for the formation of nanocomplexes. CR and mass ratio,  $MR = \frac{m^{XG}}{m^{DD}}$ , were connected by Eq. (1) [36].

$$CR = \frac{\frac{Z^{XG}}{M_{0m,mon}^{XD}}}{\frac{Z^{DD}}{M_{0m,mon}^{DD}}} \cdot MR \tag{1}$$

where Z are the charges and  $M_{\rm w}$  the molar masses per polysaccharide monomeric unit. The anionic polysaccharide XG (Fig. S1a) has two

negative charges per pentasaccharide unit, i.e.  $Z^{XG}=2$  at pH 7 and  $M_{w,mon}^{XG}=934~gmol^{-1}$  [25]. The cationic polysaccharide DD (Fig. S1b) has approximately half a positive charge per anhydroglucose unit, i.e.  $Z^{DD}=0.55~and~M_{w,mon}^{DD}=217~gmol^{-1}$  at pH 7 [33,37]. XG concentration was kept constant at 0.03 mg/mL. To prepare the NCs solutions, water was added first, followed by XG and, lastly, DD. The NCs solutions of total volume 1 mL were stirred momentarily. NCs prepared while XG was at its thermally denatured state (den-NCs) were obtained by heating the separate stock solutions at 80 °C for 30 min and mixing them immediately so that the complexation was achieved at elevated temperature. The solutions were left to cool at room temperature. The same treatment was applied to solutions of XG- and DD-only for comparison.

#### 2.1.3. Preparation of PGM/ALG beads

Regarding the preparation of PGM/ALG beads, mixed stock solutions of PGM and ALG were prepared in sterile and non-pyrogenic water at concentration ratios PGM/ALG of 5:20, 10:20, 20:20 and 40:20, with ALG concentration fixed at 20 mg/mL. The preparation protocol of Dinu et al. [42] was followed with minor modifications. Droplets of the PGM/ALG stock solution were injected into a 3 % w/v calcium chloride (CaCl<sub>2</sub>) solution by a syringe equipped with a custom-made tip of 1 mm diameter. Hydrogel beads from ALG with immobilized PGM were instantly formed in the salt solution. The beads were magnetically stirred to harden for 30 min and then were gathered and soaked in distilled water preceding their examination and evaluation experiments. Following the notation of the PGM/ALG stock solutions, beads were notated as 5:20, 10:20, 20:20 and 40:20 respectively. Control ALG beads were obtained in the same manner by a stock solution of ALG at 20 mg/mL. All collected beads were stored at 4 °C.

#### 2.1.4. Sample preparation for TEM

For transmission electron microscopy (TEM) experiments, sample concentrations higher than 1 mg/mL are usually preferred to obtain representative images. Therefore, a rotary evaporator operating at 45 °C and at 80 RPM under vacuum was utilized to evaporate part of the solvent and increase the total polymer concentration,  $C_p(=C_{XG}+C_{DD})$ , of the initially prepared NCs solutions. NCs with CR 0.4 and 2.5 with total polymer concentration after evaporation of 1.2 and 0.8 mg/mL, respectively, were tested. These two NCs were chosen as they had distinctively different compositions and properties as discussed in Sections 3.1 and 3.2. The NCs were examined by dynamic and static light scattering measurements before and after their introduction in the rotary evaporator to verify their structural integrity.

### 2.1.5. Sample preparation for interaction experiments with ANS, pyrene and PGM/ALG beads

For experiments of interactions of the NCs with ANS, NCs solutions were used both as prepared and diluted so that the concentration of XG in the tested solutions was 0.012, 0.018, 0.024 and 0.03 mg/mL. Ten  $\mu L$  of ANS dispersion (5 mM) in distilled water was added to 1 mL of the prepared solutions and the mixtures were kept for 24 h at 4 °C to equilibrate. For hydrophobicity experiments with pyrene, 2  $\mu L$  of pyrene solution in acetone at 1 mM were added to as-prepared NCs solutions (1 mL) and the samples were stored for 24 h at 4 °C to reach equilibrium [41]. The relative hydropathy of the NCs was estimated from the intensity ratio  $I_1/I_3$  in the FS spectrum of pyrene. The first (with FS intensity  $I_1$ ) and the third peak (with FS intensity  $I_3$ ) are located at 372 nm and 383 nm respectively. A polar environment is signified by  $I_1/I_3$  ratio around 1.9, whereas a non-polar environment is denoted by values close to 1.0 [43,44].

For experiments of interactions between NCs and PGM, PGM (5 mg/mL) solution in distilled water was added by titration to as-prepared NCs solutions (1 mL) to obtain PGM concentrations of 0.02, 0.04, 0.08, 0.2, 0.4 and 0.8 mg/mL respectively. For interaction experiments of the NCs with PGM/ALG and ALG beads, two beads were added to as-prepared

NCs solutions (1 mL) and remained at the bottom of the quartz cell without interfering with the incoming laser beam.

#### 2.1.6. Encapsulation of $\beta$ -C

For the  $\beta\text{-C}$  encapsulation experiments, the stock solutions of  $\beta\text{-C}$  were prepared in acetone at 8 mg/mL. The stock solution was sonicated for 2 min and stored in a shaded place at 4 °C to equilibrate. The concentration of the added  $\beta\text{-C}$  in the NCs solutions (1 mL) was equal to 40 % of  $C_p$  to obtain an adequate signal from the absorbance spectra. The resulting mixtures were stored in a fume cupboard for the acetone to volatilize, followed by gentle agitation overnight at room temperature. Thermal heating was not applied for the evaporation of acetone due to the sensitivity of  $\beta\text{-C}$  to heat exposure which can lead to its degradation [45–47]. Excess  $\beta\text{-C}$  was isolated from the NCs solution by introducing 200  $\mu\text{L}$  of n-hexane and briefly vortexing. A 20  $\mu\text{L}$  portion of the resulting supernatant n-hexane phase was then diluted with additional n-hexane and subjected to UV–Visible analysis to determine the quantity of the unencapsulated bioactive compound present [40].

All experiments were performed at 25  $^{\circ}\text{C}$  at least in triplicate. Presented uncertainties are derived as standard deviation from the mean values.

#### 2.2. Static and dynamic light scattering

A standard ALV multi-angle light scattering (LS) instrument was utilized for static and dynamic light scattering (SLS and DLS) measurements. The experiments were conducted by utilizing an ALV-CGS-3 goniometer and an ALV-5000/EPP multi-tau digital correlator with a He—Ne laser operating at  $\lambda=632.8$  nm. In SLS, the Rayleigh ratio R(q) is obtained by reducing the time-averaged scattered intensity  $\langle I(q) \rangle$  [48]. In Eq. (2) the relation between the form factor P(q) and R(q) is established. M is the molar mass, K is the LS contrast factor (Eq. 3), q is the scattering wave vector (Eq. 4), and c is the total concentration of the solution. In Eq. (4) the scattering angle is denoted by  $\theta$ , the solvent's refractive index by  $n_{o}$ , and the laser's wavelength by  $\lambda$ . In Eq. (3) the Avogadro number is denoted by  $N_{A}$  and the refractive index increment of the solute and solvent system by  $\frac{\partial n}{\partial r}$ .

$$\frac{\mathrm{Kc}}{\mathrm{R(q)}} = \frac{1}{\mathrm{MP(q)}} \tag{2}$$

$$K = \frac{4\pi^2 n_o^2}{N_h \lambda^4} \left(\frac{\partial n}{\partial c}\right)^2 \tag{3}$$

$$q = \frac{4\pi n_o}{\lambda} \sin\left(\frac{\theta}{2}\right) \tag{4}$$

The refractive index increments of XG, DD and PGM were  $\left(\frac{\partial n}{\partial c}\right)_{XG}=0.155\,\text{mL/g}$  [25,49],  $\left(\frac{\partial n}{\partial c}\right)_{DD}=0.15\,\text{mL/g}$  [50,51] and  $\left(\frac{\partial n}{\partial c}\right)_{PGM}=0.165\,\text{mL/g}$  [52] respectively. By utilizing Eq. (5), the mean values of  $\frac{\partial n}{\partial c}=0.16\,\text{mL/g}$  including PGM ( $C_{PGM}\neq 0$ ) and  $\frac{\partial n}{\partial c}=0.15\,\text{mL/g}$  omitting PGM ( $C_{PGM}=0$ ) were used for the respective experiments.

$$\begin{split} \frac{\partial n}{\partial c} &= \frac{C_{XG}}{C_{XG} + C_{DD} + C_{PGM}} \left( \frac{\partial n}{\partial c} \right)_{XG} + \frac{C_{DD}}{C_{XG} + C_{DD} + C_{PGM}} \left( \frac{\partial n}{\partial c} \right)_{DD} \\ &+ \frac{C_{PGM}}{C_{XG} + C_{DD} + C_{PGM}} \left( \frac{\partial n}{\partial c} \right)_{PGM} \end{split} \tag{5}$$

The form factor P(q) in Eq. (2) was calculated using the modified Guinier approximation (Eq. 6), where  $R_g$  is the radius of gyration. To fit the entire series of the Guinier plots a quadratic approximation with respect to  $q^2$  was incorporated [40,53,54].

$$\frac{R(q)}{Kc} = M \cdot e^{-\frac{1}{3}q^2 R_g^2 + B(q) \cdot \left(q^2\right)^2} \tag{6}$$

In DLS, the time-autocorrelation function  $g_2(q,\tau)$  of the scattered

light intensity is linked to the scattered field autocorrelation function  $g_1(q,\tau)$  via the Siegert relation [55,56]. The Stokes-Einstein equation (Eq. 7) is used to calculate the hydrodynamic radii  $R_h$  through the diffusion coefficients D, with  $k_B$  the Boltzmann constant, T the sample temperature and  $\eta$  as the solvent viscosity. The CONTIN algorithm was used to extract the distributions of hydrodynamic radii at  $\theta=90^\circ.$ 

$$R_{h} = \frac{k_{B}T}{6\pi\eta D} \tag{7}$$

#### 2.3. Electrophoretic light scattering

A Zetasizer Nano-ZS by Malvern Instruments Ltd. was used to perform electrophoretic light scattering (ELS) measurements. Under the Smoluchowski approximation, Henry's function is constant and the  $\zeta$ -potential values can be evaluated [57,58]. The apparatus measures the electrophoretic mobilities and converts them into a  $\zeta$ -potential distribution. Measurements were taken at a fixed back scattering angle  $\theta=173^\circ.$  To estimate the mean value and standard deviation of the  $\zeta$ -potential, ten measurements were collected at room temperature.

#### 2.4. Fourier transform infrared spectroscopy

A Bruker Equinox 55 device equipped with an attenuated total reflectance (ATR) diamond accessory was utilized to perform Fourier-transform infrared spectroscopy (FTIR) measurements. A few droplets (8–12 mL in volume) of the solutions were put on the middle of the sample holder and dried while being continuously exposed to nitrogen gas. Every spectrum was captured at least twice, yielding 64 scans with a 4 cm<sup>-1</sup> resolution in the 500–5000 cm<sup>-1</sup> range.

A Python code for the nonlinear least-squares method, which establishes the superposition of Gaussian peaks, was utilized to access possible PGM-ALG interactions in the PGM/ALG beads matrix by deconvoluting the respective FTIR spectra from 1800 to 1500 cm $^{-1}$ . The absolute weight  $G_{i}$ , the standard deviation  $\sigma_{i}$ , and the position  $x_{o,i}$  of each Gaussian peak comprise the general formula, i.e.  $f_{i}(x)=$ 

 $\frac{G_i}{\sigma_i\sqrt{2\pi}}e^{-\frac{\left(X-X_{0,i}\right)}{2\sigma_i^2}}$ . To aid in the algorithm's convergence, initial conditions were chosen for each of the three later parameters based on the experimental data of the FTIR spectra [41].

#### 2.5. Fluorescence spectroscopy

A Jobin Yvon-Spex Fluorolog-3 spectrofluorometer with a double-grating excitation and a single-grating emission was used to perform fluorescence spectroscopy (FS). A Xenon lamp was the light source of the device. The excitation wavelengths employed were  $\lambda=370$  nm for ANS and  $\lambda=330$  nm for pyrene. For ANS and pyrene the range of spectra recorded was 390–700 nm and 350–500 nm respectively. Slit size was set to 2 nm and integration time was set to 0.5 s for all measurements.

#### 2.6. UV-Visible spectroscopy

A Perkin-Elmer Lambda 19 UV–Vis-NIR spectrophotometer was utilized to record UV–Visible (UV–Vis) absorbance spectra. Samples were placed inside a 1 cm path length quartz cuvette holding 3 mL total volume. Measurements were conducted for wavelengths between 200 and 800 nm. The maximum intensity of PGM was reported at 258 nm, while  $\beta$ -C absorbance spectra had peak maxima at 423, 450 and 478 nm. In the case of  $\beta$ -C, the peak at 450 nm was the prominent one and the one used for the analysis of the respective spectra.

#### 2.7. Transmission electron microscopy

Transmission electron microscopy (TEM) micrographs were obtained with a Tecnai G2 Spirit Twin 12 microscope (FEI, Czech

Republic). A total of 3  $\mu$ L from each sample were placed on an electron microscopy grid coated with an electron-transparent carbon film. The samples were dried on the grid by incorporating a fast-solvent-removal method [59] followed by negative staining with uranyl acetate (UA) [60]. A total of 120 particles across multiple TEM images of each sample were identified and analyzed using ImageJ to determine the mean radius,  $R_{TEM}$ , and the standard deviation,  $\Delta R_{TEM}$ .

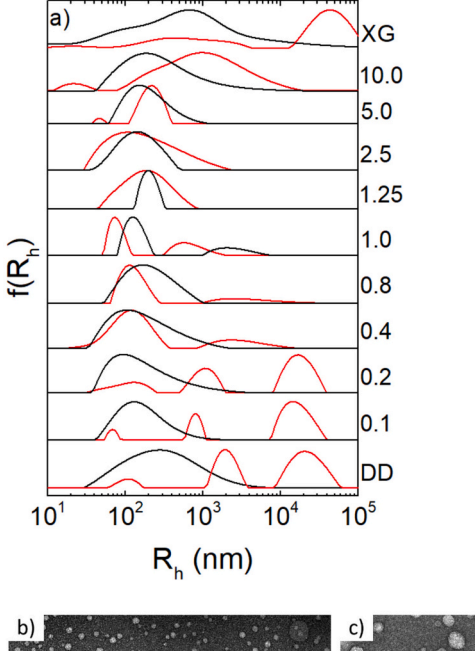
#### 3. Results and discussion

#### 3.1. Morphological and structural properties of XG/DD NCs

Complexation of XG with DD in aqueous solutions was investigated in a wide range of charge ratios  $CR = \frac{[-]}{[+]}$  from 0.1 to 10. The concentration of XG (0.03 mg/mL) was kept fixed near the overlap concentration of XG so that the effects of semi-dilute solution structure and dynamics were negligible. In our previous studies we have investigated the significant viscoelastic effects [22,23] and self-similar structure of interconnected XG chains [22] in the semidilute regime. Complexation with DD at this low XG concentration reduced the interactions and clustering between NCs allowing for a straightforward interpretation of the DLS and SLS data. Complexation was additionally investigated in the thermally denatured state of XG. At elevated temperature the helical structure of XG is destabilized and XG obtains its coil conformation [61]. In this state the side chains are freer to interact with other molecules. Therefore, a different complex formation in comparison with complexation in the native state is expected. Differences have previously been observed in the association of XG with a cationic surfactant. XG sidechains were found to associate more intensely with the surfactant in the XG's denatured state, compromising its double-helix formation [24].

The size distributions of the biopolymers alone and their mixtures are presented in Fig. 1a. The XG solutions contained a broad distribution at the native state because of the interchain interconnections [22]. In the thermally treated case, another population with large size appeared. This is explained by the fact that when XG solutions are heated to the denatured state and subsequently cooled, the double-helix formation is more effective and leads to a higher degree of association [23,62]. In DD a broad distribution appeared between 100 and 1000 nm and higher sizes were found in the thermally treated sample. These large sizes reflect the intrinsically hydrophobic nature of DD which apparently induces aggregation. Temperature increase may cause dissociation of intramolecular hydrophobic domains which may be followed by more intermolecular hydrophobic associations upon cooling.

At CR = 10, at the CR extreme, where XG content is maximum, the size distributions were still broad as in XG alone. However, they were narrower and shifted to lower Rh in comparison to XG alone. This is a sign of the complexation of the two components. The cationic DD neutralizes (or screens) the negative charges of XG reducing intramolecular repulsions in XG and, thus, causing it to adopt a more compact conformation. Notably in the case of den-NCs complexation greatly reduced the double-helix interconnected aggregates possibly by extensively occupying XG side chains in the denatured state and not allowing their reformation upon cooling. This result is reminiscent to the one of XGcationic surfactant complexes where complexation with denatured XG resulted in lower moduli and more compact complexes [24]. At CR = 5, 2.5 and 1.25 the size distributions were well below the  $\mu m$  scale with peaks at 100-200 nm. Therefore, in this CR regime NCs and den-NCs of well-defined size distributions are found. At CR = 0.1 and 0.2, at the other end of CR, where DD content is maximum, the size distributions shifted to slightly lower values, in comparison to DD alone, with Rh at about 200 nm which signifies the electrostatic interaction with XG and the shrinkage and/or partial dissociation of the primary DD aggregates. For complexation at the denatured state the peak of DD at 20 µm persisted while the one at 2  $\mu$ m shifted to 1  $\mu$ m or lower. At CR = 0.4 a single peak for NCs and a main peak for den-NCs appeared near 100 nm. For



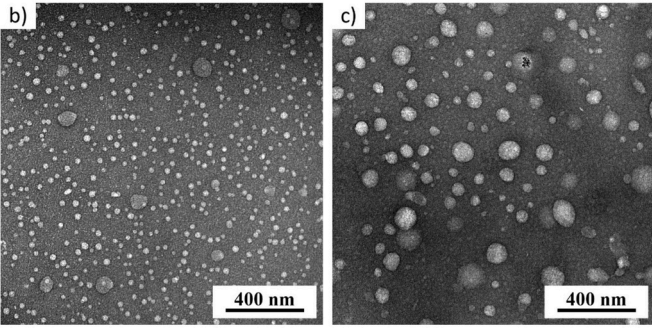


Fig. 1. a) Hydrodynamic radius distributions from CONTIN analysis at  $90^{\circ}$  of thermally untreated (black) and treated (red) XG and DD alone and XG/DD NCs (black) and den-NCs (red) for all CRs. TEM micrographs of XG/DD NCs with CR b) 0.4 and c) 2.5.

den-NCs another broad peak appeared above 1  $\mu m$  showing interconnection and clustering effects of the complexes. A qualitatively similar picture was observed at CR =0.8 where the population above 1  $\mu m$  was diminished. Apparently, clustering between NCs expected from XG interconnections and DD hydrophobic contacts was limited by the strong electrostatic interaction that takes place near the point of nominal stoichiometric charge neutrality. At CR =1 some clustering was evident at about 1  $\mu m$ . However, strong relatively narrow peaks at about 100 nm showed the presence of NCs and den-NCs. Therefore, well-defined NCs and den-NCs were also identified at CR between 0.4 and 1. The size distributions of XG/DD complexes, the appearance of well-defined NCs and relevant interpretations for the whole range of CR are summarized in Table 1. Representative field autocorrelation functions are presented and discussed in the Supporting Information (Fig. S2).

In Fig. 2 Guinier plots of the complexes are presented. The Rayleigh ratio of XG and DD alone (not shown) were lower than the ones of NCs and den-NCs in all cases except from CR=0.1. The excess scattered intensity for the mixtures proves the presence of complexes and supports the conclusion for well-defined NCs and den-NCs at CR=0.4-5 drawn from DLS. The quadratic q-dependence (Eq. 6) of the SLS profiles of the NCs and den-NCs suggests possible internal spatial correlations or polydispersity effects [40].

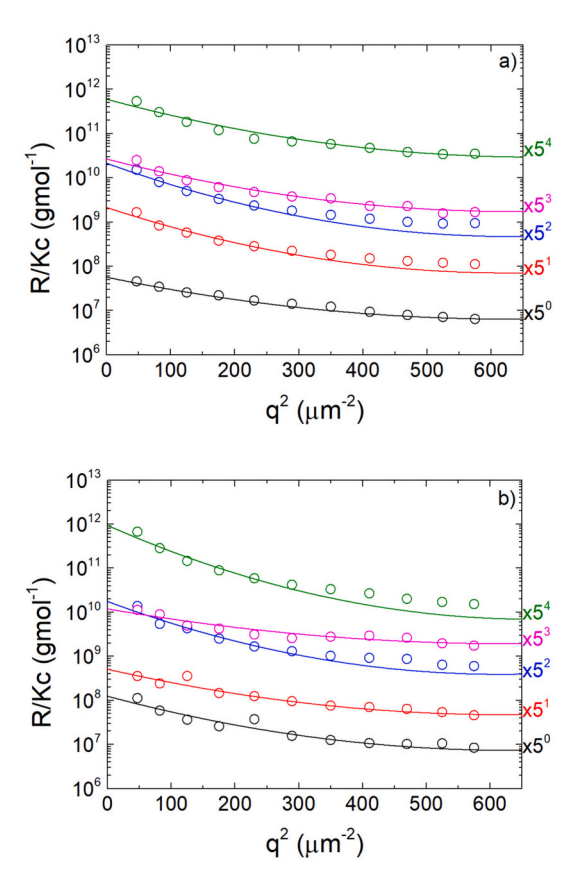
The formation of nanoparticles was verified by TEM (Fig. 1b and c). The NCs exhibited predominantly spherical shape, with radii ranging from 10 to 110 nm and mean 37  $\pm$  20 nm for CR 0.4 (Fig. S3a) and from 10 to 300 nm and mean 52  $\pm$  38 nm for CR 2.5 (Fig. S3b). Differences in

Table 1
Synopsis on the influence of CR on the hydrodynamic radii distribution and in XG/DD NCs and den-NCs.

CR	NCs	den-NCs	Key observations/ interpretation
0 (DD)	Broad size distribution 100 nm – 1 μm	Sizes at about 2 and 20 µm observed.	Hydrophobic contacts induce aggregation. Enhancement by thermal treatment.
0.10 0.20	Sizes slightly lower than DD (~200 nm).	Population at 20 $\mu m$ persists. Size at 2 $\mu m$ shifts to 1 $\mu m$ and lower.	Shrinkage/partial dissociation of DD aggregates due to electrostatic interaction with XG. In den-NCs, larger aggregates persist.
0.40	Single peak near 100 nm.	Main peak near 100 nm and broad peak above 1 μm.	Well-defined NCs and den-NCs. Broad peak >1 μm in den-NCs shows interconnection and clustering effects of complexes.
0.80	Single peak near 100 nm. Contributions above 1 µm diminished.	Main peak near 100 nm. Reduced population above 1 μm.	Well-defined NCs and den-NCs. Clustering is limited by strong electrostatic interactions near nominal stoichiometric charge neutrality.
1.00	Narrow peak ${\sim}100$ nm and some clustering at ${\sim}1~\mu m.$	Narrow peak $\sim$ 100 nm and some clustering at $\sim$ 1 $\mu$ m.	Well-defined NCs and den-NCs.
1.25 2.50 5.00	Single peak at 100–200 nm.	Single peak at 100–200 nm.	Well-defined NCs and den-NCs.
10.0	Narrower size distributions shifted to lower $R_h$ (~200 nm) in comparison to XG.	Broad size distribution at $\sim 1$ $\mu m$ .	More compact conformations of XG caused by DD. In den-NCs, DD likely prevents reformation of double helices upon cooling.
∞ (XG)	Broad distribution around 800 nm	Additional population above 10 µm	Double helix-formation which is enhanced by thermal treatment

sizes and size distributions between TEM and DLS results could be attributed to two main reasons. Firstly, DLS yields intensity-weighted size distributions and therefore is strongly affected by the presence of larger particles, while TEM yields number-weighted distributions. Secondly, the fast-solvent-removal method in TEM stabilizes the sample in the dried state (i.e. in the absence of solvent, as described elsewhere [59]), whereas DLS probes the solution morphology [63]. Notably, TEM shows the formation of spherical nanoparticles. XG is a long and rigid polysaccharide and elongated primary complexes should be expected as explained in the following discussion. However, the aggregation of the primary complexes apparently leads to spherical particles. The shape factors  $\rho$  for the NCs determined by LS methods ranged between 0.7 and 1.4 designating the possible spherical particles and the microgel morphology present.

The  $R_h$  of the NCs and den-NCs were between 100 and 200 nm with a weak increase up to CR=1 (Fig. 3a) and the PDI values ranged between approximately 0.25 and 0.4. There was a significant increase at higher CRs. In the case of multiple peaks in CONTIN analysis (Fig. 1a) the peak with  $R_h$  below 1000 nm was used for the NCs and den-NCs of Fig. 3a. An increase near charge neutrality conditions is expected as the electrostatic interactions between the complexes are diminished and large aggregates tend to form [64]. The increase at CR>1, where XG was in excess, indicates an asymmetry that arises by the fact that XG has the ability for XG-XG interconnections. The XG segments that are unassociated with DD increase in number as CR increases. Therefore, XG may



**Fig. 2.** Selected Guinier plots of XG/DD a) NCs and b) den-NCs with CR 0.4 (black), 0.8 (red), 1.25 (blue), 2.5 (magenta) and 5 (olive). Fitted lines of the modified Guinier approximation (Eq. 6) are included. Data sets were separated from each other for clarity by using different multiplication factors which are displayed on the right side of the graphs.

have more free segments to create interconnections. The effect was indeed stronger in den-NCs where XG can create more interchain double-helices. One may assume that the NCs at  $\mathrm{CR}>1$  contain complexes that are connected not only by charge effects but also by XG double-helix interconnections. The mass of the complexes (Fig. 3b) increased strongly at low CR and weakly at high CR, indicating that at  $\mathrm{CR}>1$  additional aggregation is loose. Consequently, the radius of gyration (Fig. 3c) did not change strongly by the increase of CR.

The surface potential of the NCs changes from positive (25 to 35 mV) to negative (-20 to -30 mV) at CR between 1 and 1.25 (Fig. 3d), hinting the presence of the charge neutralization ratio being between these two values. This may be connected to the rigid conformation of XG and the presumably elongated primary complexes. In this arrangement DD chains may accumulate in the exterior of the primary complexes so that their charge affects  $\zeta$  more strongly than the XG chains. In polyelectrolyte complexes ion pairing between the oppositely charged polyelectrolytes at non-stoichiometric CR results in primary complexes that consist of a charged hydrophilic corona and a charge neutralized core [36,65]. The coronas consist of segments of the polyelectrolyte in excess, and the cores consist of the mixture of the two polyelectrolyte segments. Scaling theory predicts that for flexible polyelectrolytes of different charge densities and lengths [66]. For a longer polyanion of higher charge density in comparison to the polycation cylindrical primary complexes are expected where the polyanion is elongated and the polycation forms a "coat" around it. Den-NCs showed higher absolute values of ζ. Possibly the surface of the den-NCs was more densely packed than the one of NCs as the complexation of DD with the XG side-chains. In addition, den-NCs have positive surface potential for CR 1.25 and 2.5 contrary to NCs. This may be attributed to the enhanced presence of

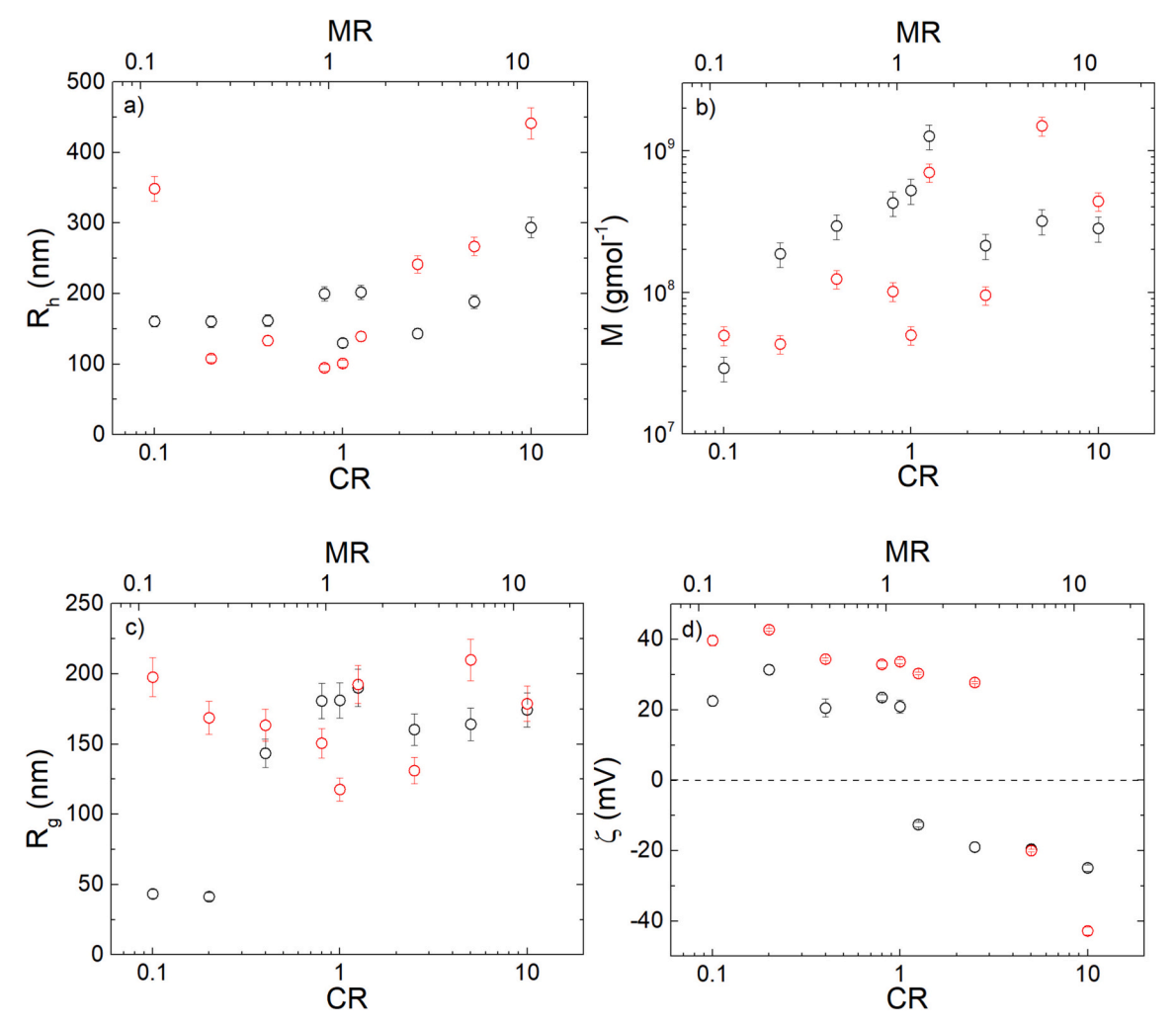


Fig. 3. a) Hydrodynamic radius  $R_h$  (CONTIN analysis at  $90^\circ$ ), b) apparent mass M, c) radius of gyration  $R_g$  and d)  $\zeta$ -potential of XG/DD NCs (black) and den-NCs (red) in relation to their respective CR and MR.

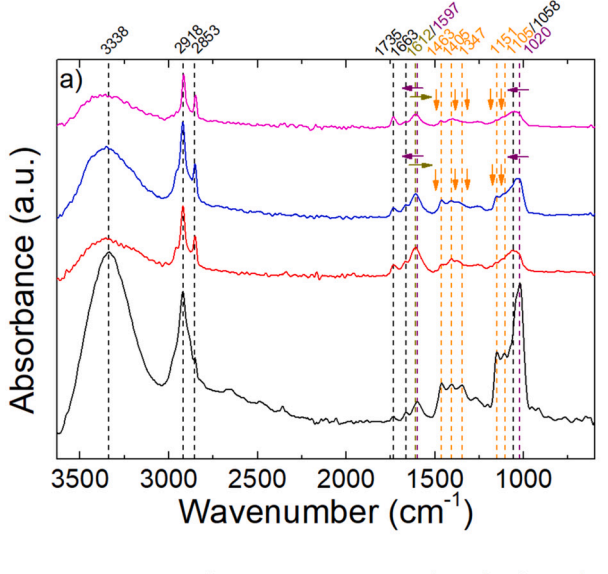
elongated primary complexes (due to more interchain double helices) and consequently to stronger effect of DD on surface potential.

According to Le Cerf et al. [33], the charge neutralization ratio of DD and carboxymethyl pullulan complexes was credited to the deprotonation and inaccessibility of quaternary amino group due to the pH dependent protonation [34] and the tertiary amino group enveloping the quaternary one. Furthermore, in the study of Hugerth et al. [67] on the complexation of chitosan and carrageenan the stoichiometric deviation was credited to the aggregation tendency of the compounds which led to the inaccessibility of the charges present on the polymeric chain. Additional factors include the charge density differences between the polyelectrolytes [68,69], the macromolecular sizes in the solution [70] and the number of charged side group units in the polysaccharide chain [69]. In the present study, the reported deviation from the nominal charge neutralization ratio was attributed to the difference in the charge density of the polysaccharide chains, the relative position of the opposite charges, as well as the rigidity and aggregation tendency of XG macromolecules.

FTIR spectra (Fig. 4) were used to decipher the functional chemical groups (see Section S4 in Supporting Information) and the possible interactions between the functional groups of the two polysaccharides. The slight shifts of 12 cm<sup>-1</sup> towards larger and of 4 cm<sup>-1</sup> towards smaller wavenumbers in the peaks at 1596 (N—H bending of DD) and 1612 (C=O stretching of XG) cm<sup>-1</sup> (Fig. 4a) respectively may indicate the complexation between the two biopolymers, as it corresponded to charged groups with charges on both polysaccharides. However, the

observed peaks at ~2850 cm<sup>-1</sup> (O-H stretching, N-H stretching and C-H stretching) for NCs and den-NCs (Fig. 4b) have exhibited no alternations or shifts despite the complexation of the two polysaccharides. The merging of the peaks at  $1663 \text{ cm}^{-1}$  and  $1603 \text{ cm}^{-1}$  (C=O stretching of XG and N-H bending of DD) reported only after thermal treatment suggested conformational changes due to high temperatures, rather than electrostatic complexation. Additionally, the reduction of the peaks' intensity in relation to the FTIR spectra of XG and DD alone (Fig. 4a) at 1463 cm<sup>-1</sup> (N—H deformation of DD) [71], 1405 cm<sup>-1</sup> (O—H bending of XG) and 1347 cm<sup>-1</sup> (O—H bending of alcohol in DD) showed possible interactions between the two suggesting conformational changes of their chains. Moreover, the critical reduction of the peaks at 1105 cm<sup>-1</sup> and the reduction of the peak at 1151 cm<sup>-1</sup> (C—O stretching of alcohol and C-N stretching of amine groups in DD) are strong indicators of the complexation between the two biopolymers. The shift of more than 10 cm<sup>-1</sup> towards larger wavenumbers in the peak at 1021 cm<sup>-1</sup> (C—N stretching of DD) for both NCs and den-NCs could have also indicated the formation of the NCs and could be related to the possible conformational changes of the amine group and potentially the ethyl group in the side chain of DD during the complexation process.

The stability of the NCs was tested after a period of 30 days. NCs with CR 0.1, 0.2, 0.8, 2.5 and 5 exhibited narrower size distributions, but with larger radii of 200–400 nm (PDI  $\sim$  0.2–0.4) (Table 2 and Fig. S4). NCs with CR 0.4 and 10 showed two distinct populations around 100–1000 nm (PDI  $\sim$  0.35), while CR 1 showed wider size distributions around radii of 200 nm (PDI  $\sim$  0.2). Den-NCs with CR 0.4, 0.8, 1 and



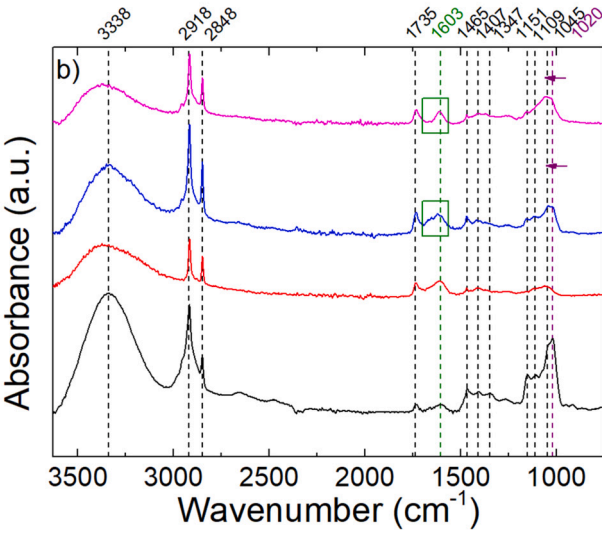


**Fig. 4.** FTIR spectra of DD alone at 0.3 mg/mL (black), XG alone at 0.03 mg/mL (red) and XG/DD a) NCs and b) den-NCs with CR 0.4 (blue) and 2.5 (magenta). Arrows pointing along the wavenumber axis indicate peak shifting towards larger (purple) and smaller (dark yellow) wavenumbers. Arrows pointing along the absorbance axis indicate relative intensity reduction (orange). Rectangles indicate peak merging (olive). The labels and positions of the peaks have been color-marked based on the relevant changes observed.

1.25 exhibited aggregation due to the stronger presence of size distributions around 1–10  $\mu m$ , while for CR with 2.5, 5, 10 populations with ~1 µm radii possibly precipitated and size distributions around 100 nm (PDI  $\sim 0.2$ ) shrank in width. For CR 0.1 10-µm-populations precipitated and for CR 0.2 some large aggregates again precipitated and the two populations around 1-10 μm appeared as a single population. Additionally, the mean hydrodynamic radii (Fig. S5a) exhibited a similar trend with the solutions on the day of their preparation. The apparent masses for both NCs and den-NCs (Fig. S5b) displayed an upward trend, while the radii of gyration (Fig. S5c) slightly decreased due to the precipitation of larger NCs. Moreover, based on the ζ-potential values (Fig. S5d) conformational changes of the polymeric chains may account for the shift of the electric charge sign near the stoichiometric charge ratio. For the NCs, the charge neutralization ratio shifted towards higher CR, whereas for the den-NCs, it transitioned to lower CR, ranging from 1.25 to 2.5 in both cases. Overall, the reported stability of the NCs and den-NCs with non-stoichiometric CR values over the span of one month

is highly encouraging, demonstrating their potential for reliable performance in long-term applications.

#### 3.2. Interactions of XG/DD NCs with model substances

The NCs were quite hydrophilic with most values being higher than 1.5–1.6 (Fig. 5a).  $\rm I_1/I_3$  was relatively lower for NCs in comparison to den-NCs. Despite their relatively high hydrophilic behavior, it is possible they contain hydrophobic nanodomains inside charge neutralized cores and can interact with hydrophobic compounds, as well as achieving their successful encapsulation. The formation of such hydrophobic regions was credited to hydrophobic interactions of deprotonated DD groups [38], as well as to the non-polar characteristics of the charge neutralized complexed segments in the core of the NCs [36].

ANS is a FS probe for the quantification of the surface hydrophobicity of self-assembled amphiphilic nanoparticles [72], hydrophobically modified polysaccharides [73] and proteins [74,75]. The FS intensity in XG solutions was found to be very weak and independent of XG concentration as is expected for polar environments e.g., when ANS is exposed to water (Fig. S6a). For DD alone FS was strong ( $\sim 10^6$ ) and its maximum shifted to lower intensities and slightly higher wavelengths by ~7 nm as DD concentration increased (Fig. S6b). This shows that in XG solutions there are apparently no hydrophobic domains for ANS to be incorporated in contrast to DD. The presence of ethyl groups in DD are therefore capable of creating the suitable nonpolar microenvironment for hydrophobic moieties to bind. As DD was found to self-aggregate (Fig. 1a) there are possibly hydrophobic domains made of ethyl groups that create intra- and inter-connections in DD chains. In addition, the competitive effects of DD self-association and ANS binding were possibly the reason for the decrease of FS as DD concentration increased. As DD concentration increased, the structure of hydrophobic domains was such that ANS was displaced [76].

FS of ANS showed roughly a decreasing trend as NCs concertation increases for CR 0.1 to 0.4 similarly to the case of DD solutions (Fig. S7a-c). Therefore, the presence of DD and the formation of hydrophobic domains dominated the interaction with ANS at high DD contents. For CR 0.8 and 1(Fig. S7d-e) there is an increasing trend showing that DD does not enhance its hydrophobic domains as NCs concentration increase. The hydrophobic domains increase trivially by NCs concentration allowing more ANS to be incorporated. At higher XG contents (CR > 1.25) (Fig. S7f-i) FS is low and nonvarying by NCs concentration as in the case of XG alone. In this case DD cannot form adequate hydrophobic domains for ANS or the electrostatic repulsion of ANS [75] with XG does not allow it to enter the NCs. In any case the FS of ANS reveals that DD modifies the properties of the NCs by introducing hydrophobic character. CRs 0.4 and 2.5 were chosen for the studies of β-C encapsulation and interactions with mucus mimics. These two CRs were symmetrically separated around CR = 1 and hence were considered representative of NCs with low and high DD content. Indeed, they had distinctly different features, i.e., surface charge of opposite sign (at least for the NCs) and different hydrophobic character. These features were expected to play a central role in the interactions with mucin and hydrophobic nutrients or drugs.

#### 3.3. Encapsulation of $\beta$ -C by the XG/DD NCs

 $\beta$ -C is a precursor to vitamin A and a potent antioxidant with anticancer [77,78], cardioprotective [79] and immunostimulant [80] properties. Due to its high hydrophobicity and tendency to degrade to illumination and heat exposure [47], the use of biocompatible nanoassemblies for its entrapment and delivery can increase the efficiency and effectiveness of the bioactive compound [78,79,81]. The encapsulation of  $\beta$ -C was tested for the two chosen CRs of XG/DD NCs i.e. 0.4 and 2.5. It was essential to estimate the water retention L<sub>w</sub> of  $\beta$ -C (Eq. 8) by conducting control experiments of  $\beta$ -C dispersions in water to account for free  $\beta$ -C that does not pass completely to the organic solvent.

Table 2 Stability test results of XG/DD NCs and den-NCs, as well as of samples of XG alone and DD alone before and after thermal treatment. For day 0, 15 and 30 after the day of preparation (Uncertainties:  $\delta Mw = 20$  %,  $\delta Rg = 7$  %,  $\delta Rh = 8$  %,  $\delta \zeta = 10$  % and  $\delta PDI = 8$  %).

State CR	CR	$M_w (\cdot 10^8 \text{ g/mol})$			R <sub>g</sub> (nm)			R <sub>h</sub> (nm)		ζ (mV)			PDI <sup>a</sup>			
		Day 0	Day 15	Day 30	Day 0	Day 15	Day 30	Day 0	Day 15	Day 30	Day 0	Day 15	Day 30	Day 0	Day 15	Day 30
NCs	0.10	0.29	0.32	0.32	43.4	181	174	161	518	393	22.5	17.6	14.8	0.40	0.43	0.39
	0.20	1.87	0.91	0.85	41.4	166	169	161	200	261	31.4	23.8	19.9	0.38	0.26	0.34
	0.40	2.95	1.57	1.88	143	169	178	162	233	340	20.5	19.3	21.3	0.37	0.36	0.36
	0.80	4.28	3.24	2.62	181	169	165	200	195	162	23.5	17.9	14.7	0.41	0.32	0.19
	1.00	5.25	5.87	3.33	181	176	161	130	183	181	20.9	18.7	15.9	0.32	0.29	0.21
	1.25	12.7	3.05	4.85	190	162	185	202	173	166	-12.6	-11.6	12.6	0.30	0.26	0.28
	2.50	2.14	5.35	5.93	160	174	181	143	160	163	-18.9	-15.7	-5.09	0.34	0.27	0.18
	5.00	3.19	2.83	2.97	164	173	177	189	150	188	-19.6	-16.3	-5.52	0.36	0.29	0.25
	10.0	2.83	2.48	5.86	174	157	211	254	96.5	424	-24.9	-18.5	-7.01	0.48	0.39	0.39
den-NCs	0.10	0.50	1.05	0.35	198	180	135	799	260	231	39.7	40.4	47.6	0.28	0.34	0.31
	0.20	0.43	0.65	0.13	169	129	143	108	111	91.2	42.8	41.9	41.4	0.46	0.47	0.16
	0.40	1.24	0.40	0.83	163	118	167	133	172	109	34.4	34.1	33.7	0.34	0.46	0.20
	0.80	1.02	0.52	1.89	151	129	149	116	98.5	108	32.9	30.9	27.6	0.35	0.50	0.20
	1.00	0.49	1.29	1.15	118	154	139	80.4	126	424	33.7	31.3	29.1	0.28	0.31	0.15
	1.25	7.03	1.32	1.56	192	134	140	182	146	111	30.3	28.7	26.9	0.38	0.33	0.18
	2.50	0.96	5.59	9.75	131	190	197	162	192	229	27.8	-28.7	-29.9	0.42	0.26	0.20
	5.00	14.9	11.3	6.62	210	198	190	267	285	206	-20.0	-20.6	-23.7	0.31	0.30	0.18
	10.0	4.39	1.58	1.81	179	150	147	981	202	203	-42.8	-28.9	-27.7	0.52	0.41	0.18
XG	_	0.05	0.08	0.11	_	_	_	539	667	843	-30.8	-32.7	-29.7	0.54	0.51	0.49
DD	-	0.01	0.03	0.05	166	136	125	296	355	456	46.4	46.1	42.8	0.36	0.37	0.42
den-XG	-	0.16	0.27	0.27	83.8	112	125	971	4920	2770	-28.9	-28.8	-30.0	0.35	0.37	0.46
den-DD	-	0.12	0.15	0.18	152	119	113	192	992	402	47.2	46.9	40.7	0.31	0.41	0.40

<sup>&</sup>lt;sup>a</sup> PDI values refer to the well-defined populations presented in Figs. 1a and S4.

$$L_{w} = \frac{m_{\beta-C} - m_{\beta-C,hex}}{m_{\beta-C}} \cdot 100\% = \frac{m_{\beta-C,w}^{*}}{m_{\beta-C}} \cdot 100\%$$
 (8)

In Eq. (8)  $m_{\beta\text{-C}}$  is the mass of  $\beta\text{-C}$  introduced in water,  $m_{\beta\text{-C},hex}$  is the mass of  $\beta\text{-C}$  transferred to n-hexane and  $m_{\beta\text{-C},w}^*$  is the mass of  $\beta\text{-C}$  that remains in water. In the presence of NCs, it was assumed that part of the unencapsulated  $\beta\text{-C}$  retained in the water solution, i.e.  $m_{\beta\text{-C}} - m_{\beta\text{-C},hex} = m_{\beta\text{-C},NCs} + m_{\beta\text{-C},w}^*$ , where  $m_{\beta\text{-C},NCs}$  was the encapsulated mass of  $\beta\text{-C}$ . In the last expression  $m_{\beta\text{-C},NCs}$  is the mass of  $\beta\text{-C}$  retained in the NCs. Assuming  $L_w$  is independent of the presence of NCs  $m_{\beta\text{-C},NCs}$  is expressed as in Eq. (9). Consequently, loading efficiency (LE) and the loading capacity (LC) are provided by Eqs. (10) and (11) respectively [40,82,83].

$$m_{\beta-C,NCs} = (1 - L_w) \cdot m_{\beta-C} - m_{\beta-C,hex} \tag{9}$$

$$LE = \frac{m_{\beta-C,NCs}}{m_{\beta-C}} \cdot 100\% \tag{10}$$

$$LC = \frac{m_{\beta-C,NCs}}{m_{NCs}} \cdot 100\% \tag{11}$$

The absorbance calibration curve was obtained after the dilution of the stock  $\beta$ -C solution in n-hexane (Fig. S8). In Fig. 5b–c the absorbance spectra of  $\beta$ -C in XG/DD NCs and den-NCs solutions are shown. Water retention was relatively high (~50 %) (Table 3) and was possibly attributed to vestiges of acetone in the solutions corroborated by a vaguely perceptible peak at 265 nm (not shown) in the absorbance spectra [84]. For XG/DD NCs (Fig. 5d and e), both CRs had similar LE and LC (Table 3), which was quite unexpected due to the high hydrophilicity of CR 2.5. However, pyrene molecules are not as flexible as  $\beta$ -C molecules and, thus,  $\beta$ -C was able to more readily access potential hydrophobic nanodomains inside the core of the NCs. For den-NCs, the low LE and LC values corroborate the absence of the characteristic orange tint of  $\beta$ -C in the aqueous solution in the presence of the supernatant n-hexane solution (Fig. S9b).

#### 3.4. Mucoadhesive properties of XG/DD NCs

The investigation of PGM-nanoparticle interactions is crucial for the development of drug delivery nanocarriers and the assessment of their

biocompatibility and behavior in biological systems. Prior research has investigated this behavior by utilizing, UV–Vis [85], FS [86] and LS [87,88] measurements. In our work, due to the low  $C_p$  of our solutions leading to insufficient strength of the absorbance and emission signals of the precursor compounds, we relied solely on both SLS and DLS techniques.

Size distributions of XG/DD NCs and PGM mixtures (Fig. S10) were indicative of the interactions of the NCs with PGM alone. The deviations from the distributions of NCs (Fig. 1) and PGM alone (Fig. S10), strongly suggested the mucoadhesive properties of both NCs with CR 0.4 and 2.5 [87]. For NCs with CR 0.4 the peak at 100 nm shifted to 200-300 nm or higher at 0.02 and 0.04 mg/mL added PGM. At 0.08 two peaks appeared with the larger size at 700-800 nm. At 0.2 and 0.4 mg/mL broad peaks from 100 nm to above 1 µm were found. These show that aggregates of the NCs with PGM are formed. At 0.8 mg/mL PGM two peaks appeared possibly showing that the scattering of PGM dominates although PGM alone showed two peaks at relatively higher sizes. For NCs at CR 2.5 the main peak at 200 nm shifted gradually to values up to 1 µm from 0.02 to 0.4 mg/mL PGM. At 0.8 mg/mL PGM a broad peak ranging from 100 nm to 10  $\mu m$  was found while the peaks from PGM alone were not detected. This showed that at CR 2.5 larger aggregates appeared in comparison to CR 0.4, leading to aggregates comprised of PGM and NCs, regardless of their surface charge and hydrophobicity. The aggregates at CR 2.5 are considered open-structured as SLS proves that more massive objects are formed at the length scale of the size of the NCs in the case of CR 0.4 (following discussion).

SLS experiments on NCs/PGM mixtures were additionally used to investigate the mucoadhesive properties of the NCs. Rayleigh ratios were plotted to compare the scattering strengths of the individual components with the ones from the mixtures. R(q) was modelled similarly to Eq. (6) as R(q) =  $R_0 \cdot e^{-\frac{1}{3}q^2R_g^2+B(q)\cdot \left(q^2\right)^2}$ . In Fig. 6  $R_0$  and  $R_g$  in relation to the concentration of added PGM  $C_{PGM}$  are presented. The scattered intensity of PGM-only solutions  $(R_0^{PGM})$  was significantly higher than the one of NCs alone. However, upon the introduction of PGM the total intensity of the mixtures surpassed that of PGM alone for  $C_{PGM}$  from 0.02 to 2 mg/mL showing that mucoadhesive interactions take place and can be detected by SLS in this  $C_{PGM}$  range.  $R_g$  values were in the vicinity of the ones of NCs and near the ones measured in PGM

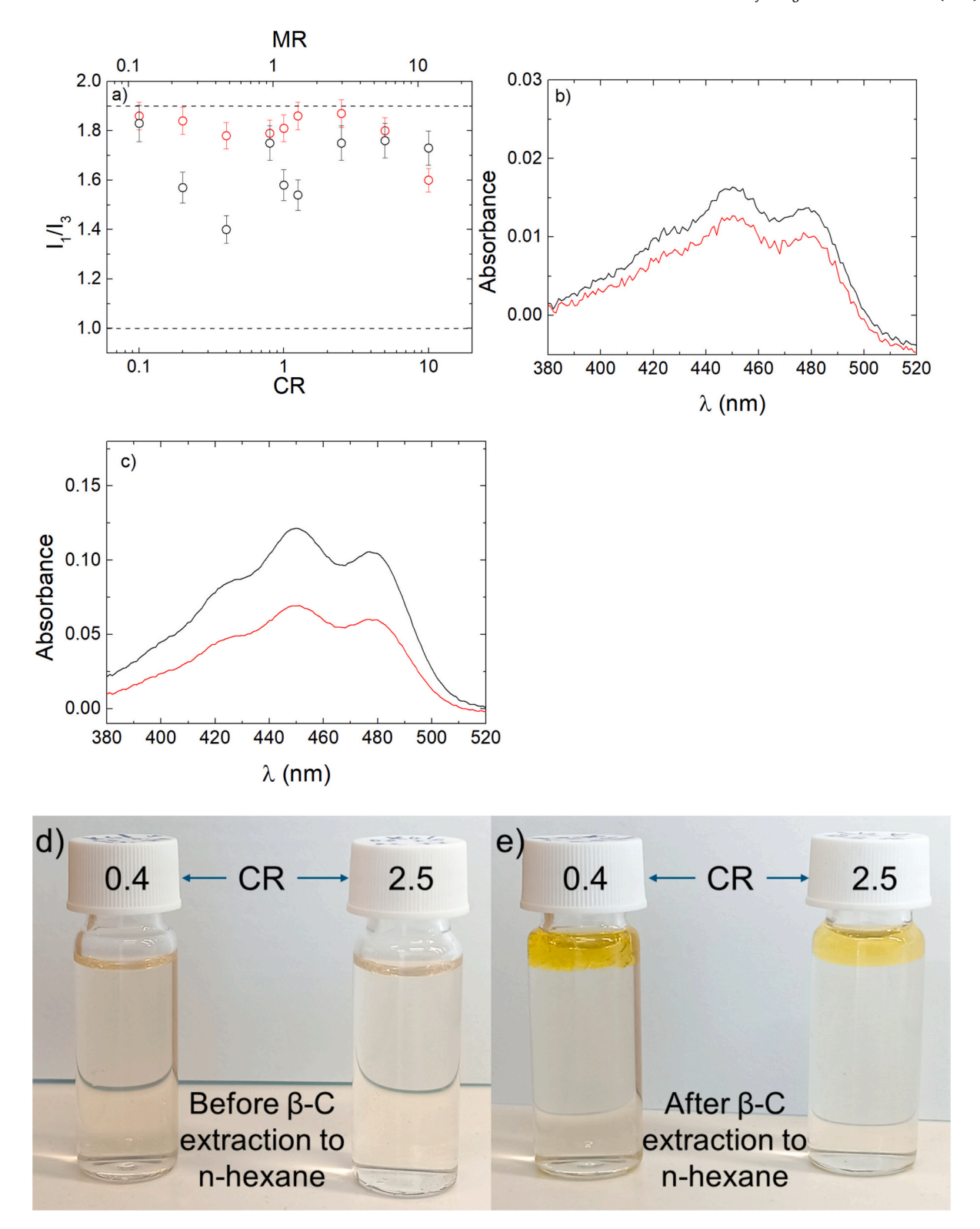


Fig. 5. a)  $I_1/I_3$  ratio derived from the respective FS spectra of pyrene for XG/DD NCs (black) and den-NCs (red), measured on the same day of preparation. UV–Vis spectra of β-C in n-hexane from XG/DD b) NCs and c) den-NCs with CR 0.4 (black) and 2.5 (red). Solutions of XG/DD NCs with CR 0.4 (left vial) and 2.5 (right vial) loaded with β-C d) before and e) after extraction of β-C to n-hexane.

alone ( $\sim$ 160–220 nm). Therefore, SLS was dominated by concentration fluctuations in the length-scale of NCs and process NCs/PGM interactions independently of DLS. In addition, the difference of  $R_0$  between NCs/PGM and NCs-only mixtures ( $R_0^{NCs/PGM}-R_0^{NCs}$ ) was also plotted (Fig. 6a) to more accurately confirm the mucoadhesive

interaction. It was indeed higher than  $R_0^{PGM}$  at  $C_{PGM}$  from 0.02 to 2 mg/mL. The interaction of PGM with positively charged NCs and den-NCs with CR 0.4 and den-NCs with CR 2.5 (Fig. 3d) was found stronger in comparison to negatively charged NCs and den-NCs. This shows that electrostatic attraction was the main driving force. However, PGM

Table 3 Water retention  $L_w$ , loading efficiency LE and loading capacity LC of  $\beta\text{-C}$  in water and untreated and thermally treated XG/DD NCs with CR 0.4 and 2.5 (relative error is  $\pm15$ %).

	CR	L <sub>w</sub> (%)	LE (%)	LC (%)
NCs	0.4	50.0	48.2	19.3
	2.5	50.0	48.8	19.5
den-NCs	0.4	50.0	4.9	2.0
	2.5	50.0	1.6	0.6

hydrophobicity [89] might also be involved in interactions with DD hydrophobic domains of the NCs. Conversely, for negatively charged NCs with CR 2.5 (Fig. 3d), the interactions may be associated with hydrogen bonding and van der Waals forces. XG is known for its strong mucoadhesion properties [29] and capability to complex with mucin [90], since uncomplexed carboxylic groups of the NCs can enhance physical entanglements and promote non-electrostatic interactions [90,91]. Electrostatic interactions could even be possible in this case if we consider that the  $\zeta$ -potential values refer to the net surface charge of the NCs and uncomplexed segments of the positively charged DD could also be present in the exterior the NCs.

To further explore the mucoadhesive properties of the NCs the mucus-mimicking system involving immobilized PGM onto ALG beads was used. PGM was immobilized within the ALG beads by physical entrapment during the gelation process and no chemical crosslinking was used [42]. The mucosa biomimetic system was initially investigated so that the immobilization of PGM was confirmed. In Dinu et al. [42] the potential immobilization of PGM was reported by scanning electron microscopy where PGM aggregates were observed on the surface of ALG beads. The immobilization of PGM on the surface of the beads was also verified by  $\zeta$ -potential measurements and the apparent change of the

surface charge in the presence of PGM. The PGM/ALG beads of that work were tested in comparison to an ex-vivo bovine tongue in flavour retention experiments. They showed qualitative agreement and were also proved effective for testing mucoadhesive polymers. In this work the immobilization of PGM was confirmed by FTIR in the bulk of the beads. The FTIR spectra of the precursor compounds and the PGM/ALG beads at different concentration ratios are presented in Fig. 7. To obtain the spectra from the bulk, the beads were crushed onto the sample holder before drying. Clear indicators of the presence of PGM in the beads (Fig. 7a) were the subtle peaks at 2852 (C-H stretching) and 1738 cm<sup>-1</sup> (C=O and N-H stretching) in the spectrum of PGM/ALG 5:20 beads. In fact, the latter peak was shifted by 10 cm<sup>-1</sup> towards higher wavenumbers which most likely indicated the conformational changes of PGM resulting from its immobilization in the hydrogel beads. Additionally, a broadened peak at 1599 cm<sup>-1</sup> (C=O stretching and O—H bending) was attributed to the combination of the peak at 1653  ${\rm cm}^{-1}$  and 1535  ${\rm cm}^{-1}$  (C=O and N-H stretching) from PGM and the peak at 1599 cm<sup>-1</sup> from ALG. Further investigation to distinguish possible PGM-ALG interactions in PGM/ALG beads was performed by deconvoluting the FTIR spectra of 5:20 PGM/ALG beads (Fig. 7c), ALG and PGM alone (not shown). Quantitative results are presented in Table 4 where characteristic peak parameters, i.e. peak center and full width at half-maximum (FWHM), are reported. PGM peaks of 1738, 1653 and 1535 cm<sup>-1</sup> shifted towards lower wavenumbers and experienced broadened peaks (apart from peak 1530 cm<sup>-1</sup> which shrank in width). These changes are indicative of possible hydrogen bonding between ALG and PGM molecules in the matrix of the hydrogel, as well as possible calcium bridging [92–94]. ALG peak of 1599 cm<sup>-1</sup> remained in place, but experienced mild broadening. While this peak broadening could also indicate possible PGM-ALG interaction, similar broadening was present at the spectrum of control ALG beads (Fig. 7a) and could be

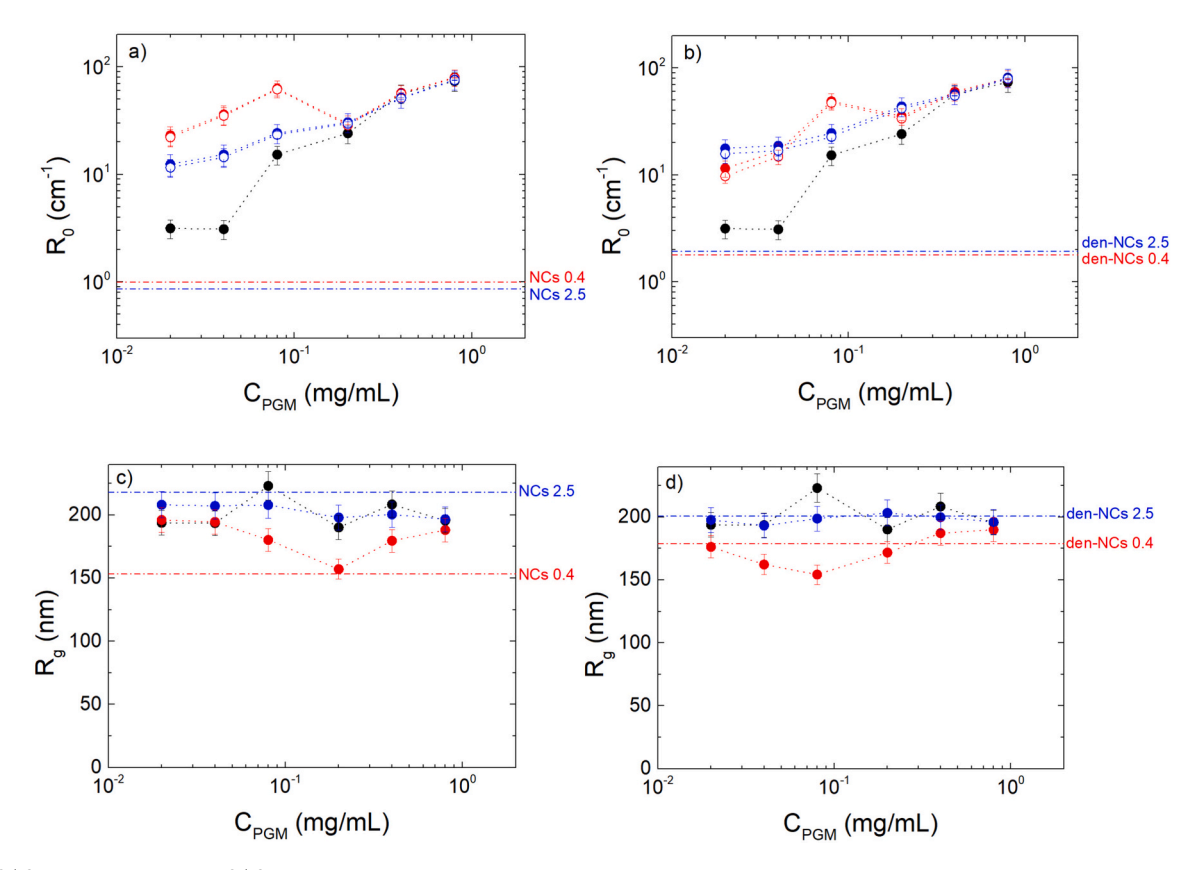
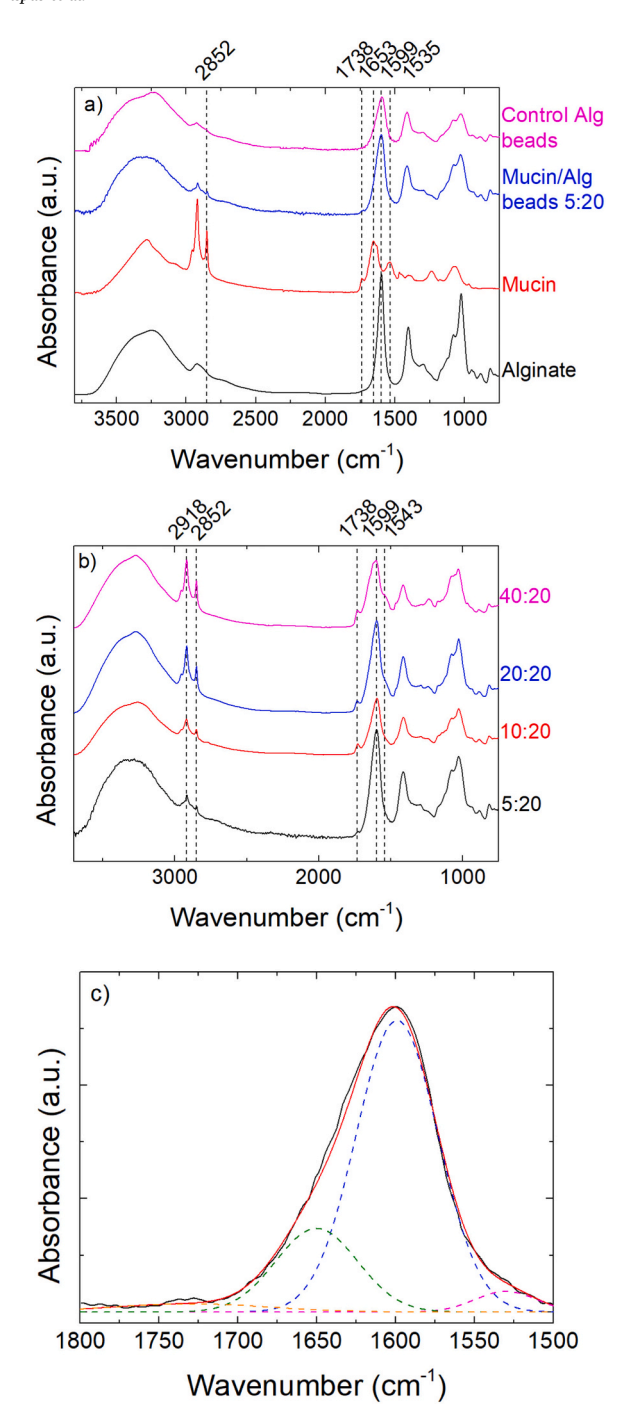


Fig. 6.  $R_0^{NCS/PGM}$  (filled circles) and  $R_0^{NCS/PGM} - R_0^{NCS}$  (open circles) for XG/DD a) NCs and b) den-NCs with CR 0.4 (red) and 2.5 (blue) and  $R_0^{PGM}$  (filled black squares). Radius of gyration  $R_g$  of PGM-only (black) and NCs/PGM mixtures of XG/DD c) NCs and d) den-NCs with CR 0.4 (red) and 2.5 (blue). The  $R_0$  and Rg values of NCs and den-NCs alone with CR 0.4 (red) and 2.5 (blue) are presented respectively as dashed-dotted lines.



**Fig. 7.** a) FTIR absorbance spectra of ALG alone (black), PGM alone (red), PGM/ALG beads of 5:20 (blue) and control ALG beads (magenta). b) FTIR absorbance spectra of PGM/ALG beads of 5:20 (black), 10:20 (red), 20:20 (blue) and 40:20 (magenta). c) Deconvolution of FTIR absorbance spectrum of 5:20 beads in the region of 1800–1500 cm $^{-1}$ . Colors: Experimental data (solid black), fitted profile (solid red) and deconvoluted peaks at 1730 (dashed orange), 1650 (dashed olive), 1599 (dashed blue) and 1530 (dashed magenta) cm $^{-1}$ .

related to the change of vibrational modes of the ALG molecules after crosslinking with calcium cations [93]. To obtain further confirmation of the presence of PGM in the beads the FTIR spectra of all four concentration ratios of PGM/ALG beads were analyzed (Fig. 7b). It was evident that the peaks at 2918 (C—H stretching), 2852 and 1738 cm<sup>-1</sup> attributed to PGM became clearer. The peak at 1599 cm<sup>-1</sup>, which was primarily attributed to ALG, underwent changes to its shape due to the

**Table 4**Comparison of the FTIR peak parameters of ALG and PGM alone and 5:20 PGM/ALG beads via deconvolution in the region of 1800–1500 cm<sup>-1</sup>.

Number of peaks	ALG alon	e	PGM alor	ie	5:20 PGM/ALG beads		
	Center (cm <sup>-1</sup> )	FWHM (cm <sup>-1</sup> )	Center (cm <sup>-1</sup> )	FWHM (cm <sup>-1</sup> )	Center (cm <sup>-1</sup> )	FWHM (cm <sup>-1</sup> )	
1.	-	-	1738	27	1730	106	
2.	-	-	1653	76	1650	63	
3.	1599	55	-	-	1599	62	
4.	-	-	1535	55	1530	48	

strong presence of the peak at 1653 cm<sup>-1</sup>. Lastly, the PGM retention (Table S1 and Fig. S11 and S12) and the macroscopic drying results of control ALG and PGM/ALG beads (Fig. S13) indicated the less immobilized PGM on the beads, the largest PGM retention it exhibits, as well as the fastest drying process (see Supporting Information).

Mucoadhesion experiments were conducted with XG/DD NCs and den-NCs with CR 0.4 and 2.5 by subjecting them to LS measurements in the presence of control ALG and 5:20 PGM/ALG beads since the latter beads exhibited the largest PGM retention (Table S1). In Fig. 8a and b the apparent M of the supernatant solutions in the absence of NCs on the

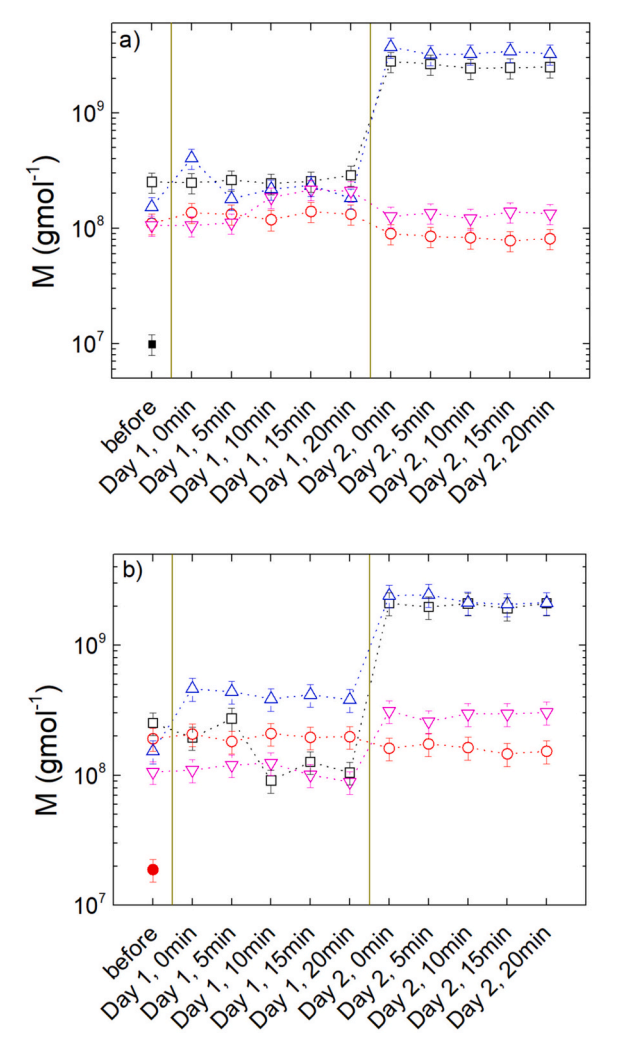


**Fig. 8.** Apparent mass M of XG/DD NCs with CR 0.4 (black) and 2.5 (red) and den-NCs with CR 0.4 (blue) and 2.5 (magenta), interacting with a) control ALG and b) PGM/ALG 5:20 beads. Filled individual points correspond to the apparent mass of the supernatant solution surrounding control ALG (black) and PGM/ALG (red) beads.

third day of preparation showed that ALG and PGM spontaneously separated from the beads and dispersed in the solution. However, their concentration was apparently very low. Compared with the scattering of PGM of known concentration, the PGM that separates from the beads was  $\sim$ 2 orders of magnitude lower than the lowest used for experiments with PGM alone. Such low PGM and conversely ALG concentrations were not expected to cause significant aggregation. In the case of control ALG beads the negatively charged NCs and den-NCs (CR = 2.5) showed a decrease in apparent M after one day (Fig. 8a). This was a sign of mild interaction where the NCs and den-NCs were attracted and immobilized by the beads. The positively charged NCs and den-NCs with CR 0.4 displayed interaction and aggregate formation on the second day, most likely due to detached ALG molecules in the excess solution (Fig. 8a). The presence of NCs and their interaction with the beads apparently caused stronger detachment of the ALG molecules in comparison to the spontaneous detachment and this way such an increase in M was possible. For PGM/ALG beads, the second day of measurements suggested strong aggregation taking place between detached PGM (and ALG) and NCs (Fig. 8b). In this case also the detachment of PGM and ALG was mainly due to the presence of NCs. Only den-CNS with CR = 2.5were found to interact mildly with the beads, i.e. being immobilized. Size distributions (Fig. S14b) further indicated the formation of aggregates and the interaction of positively charged NCs and den-NCs with CR 0.4 and only den-NCs with CR 2.5. Furthermore, the presence of narrow peaks with sizes exceeding 1 µm strongly indicated the occurrence of an interaction phenomenon (Fig. S14).

#### 4. Conclusions

The electrostatic complexation of XG and DD was investigated for the biocompatible preparation of well-defined NCs. NCs with nonstoichiometric CR exhibited tunable sizes, colloidal stability and compact morphology based on LS and TEM measurements. The ζ-potential measurements indicated a charge inversion near CR 1-1.25 which slightly deviated from the nominal charge neutralization ratio due to charge density differences between the two polysaccharides and the inflexibility and rigidity of the XG molecules. While fluorescence spectroscopy with pyrene probe indicated the highly hydrophilic nature of the NCs, the ANS probe revealed the presence of hydrophobic domains attributed to the ethyl groups of DD based on the potential displacement of ANS molecules. These domains enable the successful and highly potent encapsulation of  $\beta$ -C for native NCs. On the contrary, den-NCs exhibited significantly diminished encapsulation effectiveness, highlighting the importance of polymer segment complexation, as well as polymer conformation in nanoassemblies. Mucoadhesive experiments using PGM-only solutions and PGM-immobilized ALG beads confirmed the strong interactions of positively charged NCs with mucus analogs, primarily driven by electrostatic attraction. Notably, negatively charged NCs retained mucoadhesive potential, most likely due to XG's inherent ability to form physical entanglements and non-electrostatic interactions with mucin molecules. Conclusively, the present NCs offered a promising platform for drug delivery applications. Their colloidal properties, encapsulation efficiency and mucoadhesiveness can be effectively adjusted by the choice of CR and the thermal treatment of the two biopolymers prior to complexation. The present study provides a versatile and thorough strategy for the preparation of biocompatible nanocarriers, the optimization of their interaction with mucosal environments and the encapsulation effectiveness of model hydrophobic compounds, which can inspire the design of future biopolymeric drug nanocarriers.

#### CRediT authorship contribution statement

**Ioannis Pispas:** Writing – review & editing, Writing – original draft, Visualization, Validation, Investigation, Formal analysis, Data curation. **Ewa Pavlova:** Investigation, Formal analysis. **Miroslav Slouf:** Writing –

review & editing, Validation, Resources. **Aristeidis Papagiannopoulos:** Writing – review & editing, Visualization, Validation, Supervision, Resources, Methodology, Conceptualization.

#### **Funding**

This research received no external funding.

#### Declaration of competing interest

The authors declare that they have no known competing financial interests or personal relationships that could have appeared to influence the work reported in this paper.

#### Acknowledgements

None.

#### Appendix A. Supplementary data

Supplementary data to this article can be found online at https://doi.org/10.1016/j.ijbiomac.2025.147766.

#### Data availability

Data will be made available on request.

#### References

- Y. Luo, Q. Wang, Recent development of chitosan-based polyelectrolyte complexes with natural polysaccharides for drug delivery, Int. J. Biol. Macromol. 64 (2014) 353–367, https://doi.org/10.1016/j.ijbiomac.2013.12.017.
- [2] Yudishter, R. Shams, K.K. Dash, Polysaccharide nanoparticles as building blocks for food processing applications: a comprehensive review, Food Sci. Biotechnol. 34 (2025) 527–546, https://doi.org/10.1007/s10068-024-01695-w.
- [3] A. Plucinski, Z. Lyu, B.V.K.J. Schmidt, Polysaccharide nanoparticles: from fabrication to applications, J. Mater. Chem. B 9 (2021) 7030–7062, https://doi. org/10.1039/D1TB00628B.
- [4] A.-G. Niculescu, A.M. Grumezescu, Applications of chitosan-alginate-based nanoparticles—an up-to-date review, Nanomaterials 12 (2022) 186, https://doi. org/10.3390/nano12020186.
- [5] F.C. Moraes, L. Marcelo Forero Ramirez, R. Aid, S. Benadda, M. Maire, C. Chauvierre, J.C. Antunes, F. Chaubet, D. Letourneur, P-selectin targeting polysaccharide-based nanogels for miRNA delivery, Int. J. Pharm. 597 (2021) 120302, https://doi.org/10.1016/j.ijpharm.2021.120302.
- [6] Y. Liu, D. Chen, A. Zhang, M. Xiao, Z. Li, W. Luo, Y. Pan, W. Qu, S. Xie, Composite inclusion complexes containing hyaluronic acid/chitosan nanosystems for dual responsive enrofloxacin release, Carbohydr. Polym. 252 (2021) 117162, https:// doi.org/10.1016/j.carbpol.2020.117162.
- [7] G. Zucca, B. Vigani, C. Valentino, M. Ruggeri, N. Marchesi, A. Pascale, G. Giovilli, L. Malavasi, G. Sandri, S. Rossi, Chondroitin sulphate-chitosan based nanogels loaded with naringenin-β-cyclodextrin complex as potential tool for the treatment of diabetic retinopathy: a formulation study, IJN 20 (2025) 907–932, https://doi. org/10.2147/IJN S488507
- [8] V. Dulong, P. Thebault, C. Karakasyan, L. Picton, D. Le Cerf, Polyelectrolyte complexes of chitosan and hyaluronic acid or carboxymethylpullulan and their aminoguaiacol derivatives with biological activities as potential drug delivery systems, Carbohydr. Polym. 341 (2024) 122330, https://doi.org/10.1016/j. carbpol.2024.122330.
- [9] J. Wang, S. Asghar, L. Yang, S. Gao, Z. Chen, L. Huang, L. Zong, Q. Ping, Y. Xiao, Chitosan hydrochloride/hyaluronic acid nanoparticles coated by mPEG as longcirculating nanocarriers for systemic delivery of mitoxantrone, Int. J. Biol. Macromol. 113 (2018) 345–353, https://doi.org/10.1016/j.ijbiomac.2018.02.128.
- [10] B. Chen, C. Ai, Y. He, Y. Zheng, L. Chen, H. Teng, Preparation and structural characterization of chitosan-sodium alginate nanocapsules and their effects on the stability and antioxidant activity of blueberry anthocyanins, Food Chem. X 23 (2024) 101744, https://doi.org/10.1016/j.fochx.2024.101744.
- [11] X. Ding, Y. Xu, Y. Wang, L. Xie, S. Liang, D. Li, Y. Wang, J. Wang, X. Zhan, Carboxymethyl konjac glucomannan-chitosan complex nanogels stabilized double emulsions incorporated into alginate hydrogel beads for the encapsulation, protection and delivery of probiotics, Carbohydr. Polym. 289 (2022) 119438, https://doi.org/10.1016/j.carbnol.2022.119438.
- https://doi.org/10.1016/j.carbpol.2022.119438.
   [12] S. Mitra, A. Kundagrami, Polyelectrolyte complexation of two oppositely charged symmetric polymers: a minimal theory, J. Chem. Phys. 158 (2023) 014904, https://doi.org/10.1063/5.0128904.

- [13] V.S. Meka, M.K.G. Sing, M.R. Pichika, S.R. Nali, V.R.M. Kolapalli, P. Kesharwani, A comprehensive review on polyelectrolyte complexes, Drug Discov. Today 22 (2017) 1697–1706, https://doi.org/10.1016/j.drudis.2017.06.008.
- [14] A.D. Kulkarni, Y.H. Vanjari, K.H. Sancheti, H.M. Patel, V.S. Belgamwar, S. J. Surana, C.V. Pardeshi, Polyelectrolyte complexes: mechanisms, critical experimental aspects, and applications, Artif. Cells Nanomed. Biotechnol. 44 (2016) 1615–1625, https://doi.org/10.3109/21691401.2015.1129624.
- [15] M. Ishihara, S. Kishimoto, S. Nakamura, Y. Sato, H. Hattori, Polyelectrolyte complexes of natural polymers and their biomedical applications, Polymers 11 (2019) 672, https://doi.org/10.3390/polym11040672.
- [16] E. Pelletier, C. Viebke, J. Meadows, P.A. Williams, A rheological study of the order-disorder conformational transition of xanthan gum, Biopolymers 59 (2001) 339–346, https://doi.org/10.1002/1097-0282(20011015)59:5<339::AID-BIP1031>3.0.CO;2-A.
- [17] N.B. Wyatt, M.W. Liberatore, The effect of counterion size and valency on the increase in viscosity in polyelectrolyte solutions, Soft Matter 6 (2010) 3346, https://doi.org/10.1039/c000423e.
- [18] G. Sworn, Xanthan gum, in: A. Imeson (Ed.), Food Stabilisers, Thickeners and Gelling Agents, 1st ed, Wiley, 2009, pp. 325–342, https://doi.org/10.1002/ 9781444314724.ch17.
- [19] K. Born, V. Langendorff, P. Boulenguer, Xanthan, in: A. Steinbüchel (Ed.), Biopolymers Online, 1st ed., Wiley, 2002 https://doi.org/10.1002/3527600035. hppl5011
- [20] Y. Meng, C. Qiu, X. Li, D.J. McClements, S. Sang, A. Jiao, Z. Jin, Polysaccharide-based nano-delivery systems for encapsulation, delivery, and pH-responsive release of bioactive ingredients, Crit. Rev. Food Sci. Nutr. 64 (1) (2024) 187–201, https://doi.org/10.1080/10408398.2022.2105800.
- [21] M. Wu, J. Qu, X. Tian, X. Zhao, Y. Shen, Z. Shi, P. Chen, G. Li, T. Ma, Tailor-made polysaccharides containing uniformly distributed repeating units based on the xanthan gum skeleton, Int. J. Biol. Macromol. 131 (2019) 646–653, https://doi. org/10.1016/j.ijbiomac.2019.03.130.
- [22] A. Papagiannopoulos, K. Sotiropoulos, A. Radulescu, Scattering investigation of multiscale organization in aqueous solutions of native xanthan, Carbohydr. Polym. 153 (2016) 196–202, https://doi.org/10.1016/j.carbpol.2016.07.104.
- [23] A. Papagiannopoulos, K. Sotiropoulos, S. Pispas, Particle tracking microrheology of the power-law viscoelasticity of xanthan solutions, Food Hydrocoll. 61 (2016) 201–210, https://doi.org/10.1016/j.foodhyd.2016.05.020.
- [24] K. Sotiropoulos, A. Papagiannopoulos, Modification of xanthan solution properties by the cationic surfactant DTMAB, Int. J. Biol. Macromol. 105 (2017) 1213–1219, https://doi.org/10.1016/j.ijbiomac.2017.07.162.
- [25] A. Papagiannopoulos, A. Sklapani, Xanthan-based polysaccharide/protein nanoparticles: preparation, characterization, encapsulation and stabilization of curcumin, Carbohydr. Polym. Technol. Appl. 2 (2021) 100075, https://doi.org/ 10.1016/j.carpta.2021.100075.
- [26] Y. Zhu, X. Sun, J. Ding, F. Fan, P. Li, J. Xia, X. Luo, Y. Fang, Physicochemical and functional properties of a novel xanthan gum-lysozyme nanoparticle material prepared by high pressure homogenization, LWT 143 (2021) 111136, https://doi. org/10.1016/i.lwt.2021.111136.
- [27] A.C. Mendes, T. Strohmenger, F. Goycoolea, I.S. Chronakis, Electrostatic selfassembly of polysaccharides into nanofibers, Colloids Surf. A Physicochem. Eng. Asp. 531 (2017) 182–188, https://doi.org/10.1016/j.colsurfa.2017.07.044.
- [28] U. Afnan, K. Sharma, R. Sehgal, V. Kumar, Xanthan gum-based nanocarriers for therapeutic delivery, in: Polymeric Nanosystems, Elsevier, 2023, pp. 333–365, https://doi.org/10.1016/B978-0-323-85656-0.00008-5.
- [29] R.R. Shiledar, A.A. Tagalpallewar, C.R. Kokare, Formulation and in vitro evaluation of xanthan gum-based bilayered mucoadhesive buccal patches of zolmitriptan, Carbohydr. Polym. 101 (2014) 1234–1242, https://doi.org/10.1016/ i.carbool.2013.10.072.
- [30] V.R. Sinha, R. Kumria, Binders for colon specific drug delivery: an in vitro evaluation, Int. J. Pharm. 249 (2002) 23–31, https://doi.org/10.1016/S0378-5173 (02)00398-8
- [31] R. Abu-Huwaij, R.M. Obaidat, K. Sweidan, Y. Al-Hiari, Formulation and in vitro evaluation of xanthan gum or carbopol 934-based mucoadhesive patches, loaded with nicotine, AAPS PharmSciTech 12 (2011) 21–27, https://doi.org/10.1208/ s12249-010-9534-5.
- [32] G. Barberi, G. Biscari, V. Catania, D. Punginelli, C. Scialabba, C. Fiorica, D. Schillaci, G. Cavallaro, Thermosensitive and mucoadhesive xanthan gum-based hydrogel for local release of anti-Candida peptide, J. Drug Deliv. Sci. Technol. 100 (2024) 106054, https://doi.org/10.1016/j.jddst.2024.106054.
- [33] D. Le Cerf, A.S. Pepin, P.M. Niang, M. Cristea, C. Karakasyan-Dia, L. Picton, Formation of polyelectrolyte complexes with diethylaminoethyl dextran: charge ratio and molar mass effect, Carbohydr. Polym. 113 (2014) 217–224, https://do. org/10.1016/j.carbpol.2014.07.015.
- [34] T. Heinze, T. Liebert, B. Heublein, S. Hornig, Functional polymers based on dextran, in: D. Klemm (Ed.), Polysaccharides II, Springer Berlin Heidelberg, 2006, pp. 199–291, https://doi.org/10.1007/12\_100.
- [35] A.R. Petrovici, M. Pinteala, N. Simionescu, Dextran formulations as effective delivery systems of therapeutic agents, Molecules 28 (2023) 1086, https://doi.org/ 10.3390/molecules28031086.
- [36] H.V. Le, V. Dulong, L. Picton, D. Le Cerf, Polyelectrolyte complexes of hyaluronic acid and diethylaminoethyl dextran: Formation, stability and hydrophobicity, Colloids Surf. A Physicochem. Eng. Asp. 629 (2021) 127485, https://doi.org/ 10.1016/j.colsurfa.2021.127485.
- [37] C. Siewert, H. Haas, T. Nawroth, A. Ziller, S.S. Nogueira, M.A. Schroer, C. E. Blanchet, D.I. Svergun, A. Radulescu, F. Bates, Y. Huesemann, M.P. Radsak, U. Sahin, P. Langguth, Investigation of charge ratio variation in mRNA DEAE-

- dextran polyplex delivery systems, Biomaterials 192 (2019) 612–620, https://doi.org/10.1016/i.biomaterials.2018.10.020.
- [38] Z. Souguir, S. Roudesli, E. About-Jaudet, L. Picton, D. Le Cerf, Novel cationic and amphiphilic pullulan derivatives II: pH dependant physicochemical properties, Carbohydr. Polym. 80 (2010) 123–129, https://doi.org/10.1016/j. carbpol.2009.11.003.
- [39] M. Abid, M. Mahmood, M. Batool, S.H. Sumrra, M.F. Nazar, Biodegradable polymeric nanoparticle drug for oral delivery applications, in: Novel Platforms for Drug Delivery Applications, Elsevier, 2023, pp. 333–348, https://doi.org/10.1016/ B978-0-323-91376-8.00017-3.
- [40] A. Papagiannopoulos, E. Vlassi, Stimuli-responsive nanoparticles by thermal treatment of bovine serum albumin inside its complexes with chondroitin sulfate, Food Hydrocoll. 87 (2019) 602–610, https://doi.org/10.1016/j. foodbyd.2018.08.054.
- [41] I. Pispas, N. Spiliopoulos, A. Papagiannopoulos, Biocompatible preparation of betalactoglobulin/chondroitin sulfate carrier nanoparticles and modification of their colloidal and hydropathic properties by Tween 80, Polymers 16 (2024) 1995, https://doi.org/10.3390/polym16141995.
- [42] V. Dinu, G.E. Yakubov, M. Lim, K. Hurst, G.G. Adams, S.E. Harding, I.D. Fisk, Mucin immobilization in calcium alginate: a possible mucus mimetic tool for evaluating mucoadhesion and retention of flavour, Int. J. Biol. Macromol. 138 (2019) 831–836, https://doi.org/10.1016/j.ijbiomac.2019.07.148.
- [43] T. Wu, J. Oake, Z. Liu, C. Bohne, N.R. Branda, Probing the microenvironments in a polymer-wrapped core-shell nanoassembly using pyrene chromophores, ACS Omega 3 (2018) 7673–7680, https://doi.org/10.1021/acsomega.8b00953.
- [44] D.C. Dong, M.A. Winnik, The P y scale of solvent polarities. Solvent effects on the vibronic fine structure of pyrene fluorescence and empirical correlations with E<sub>T</sub> and Y values, Photochem. Photobiol. 35 (1982) 17–21, https://doi.org/10.1111/ i.1751-1097.1982.tb03805.x.
- [45] A. Zeb, Oxidation and formation of oxidation products of β-carotene at boiling temperature, Chem. Phys. Lipids 165 (2012) 277–281, https://doi.org/10.1016/j. chemphyslip.2012.02.005.
- [46] B.H. Chen, J.H. Huang, Degradation and isomerization of chlorophyll a and β-carotene as affected by various heating and illumination treatments, Food Chem. 62 (1998) 299–307, https://doi.org/10.1016/S0308-8146(97)00201-X.
- [47] M. Syamila, M.A. Gedi, R. Briars, C. Ayed, D.A. Gray, Effect of temperature, oxygen and light on the degradation of β-carotene, lutein and α-tocopherol in spray-dried spinach juice powder during storage, Food Chem. 284 (2019) 188–197, https:// doi.org/10.1016/j.foodchem.2019.01.055.
- [48] B. Chu, Laser Light Scattering: Basic Principles and Practise, Courier Corporation,
- [49] M. Milas, W.F. Reed, S. Printz, Conformations and flexibility of native and renatured xanthan in aqueous solutions, Int. J. Biol. Macromol. 18 (1996) 211–221, https://doi.org/10.1016/0141-8130(95)01080-7.
- [50] K. Kleemann, P. Bolduan, G. Battagliarin, I. Christl, K. McNeill, M. Sander, Molecular structure and conformation of biodegradable water-soluble polymers control adsorption and transport in model soil mineral systems, Environ. Sci. Technol. 58 (2024) 1274–1286, https://doi.org/10.1021/acs.est.3c05770.
- [51] R. Hanselmann, W. Burchard, R. Lemmes, D. Schwengers, Characterization of DEAE-dextran by means of light scattering and combined size-exclusion chromatography/low-angle laser light scattering/viscometry, Macro Chem. Phys. 196 (1995) 2259–2275, https://doi.org/10.1002/macp.1995.021960715.
- [52] L.H. Abdullah, C. Wolber, M. Kesimer, J.K. Sheehan, C.W. Davis, Studying mucin secretion from human bronchial epithelial cell primary cultures, in: M. A. McGuckin, D.J. Thornton (Eds.), Mucins, Humana Press, Totowa, NJ, 2012, pp. 259–277, https://doi.org/10.1007/978-1-61779-513-8\_16.
- [53] R. Borsali, R. Pecora, Soft-matter Characterization, Springer, 2008.
- [54] L. Øgendal, Light Scattering a Brief Introduction, University of Copenhagen, 2019.
- [55] B.J. Berne, R. Pecora, Dynamic Light Scattering: With Applications to Chemistry, Biology, and Physics, Dover Publications Inc, 2000.
- [56] M. Alexander, D.G. Dalgleish, Dynamic light scattering techniques and their applications in food science, Food Biophys. 1 (2006) 2–13, https://doi.org/ 10.1007/s11483-005-9000-1.
- [57] R.J. Hunter, Zeta Potential in Colloid Science: Principles and Applications, New paperback edition, Academic Press, London San Diego, 1988.
- [58] H. Ohshima, Electrophoretic mobility of a spherical colloidal particle in a salt-free medium, J. Colloid Interface Sci. 248 (2002) 499–503, https://doi.org/10.1006/ icis 2002 8232
- [59] Z. Černochová, V. Lobaz, L. Čtveráčková, P. Černoch, M. Šlouf, M. Filipová, M. Hrubý, J. Pánek, Encapsulating melittin from animal venom by finely tuned charge compensation with polymer carriers, Eur. Polym. J. 190 (2023) 111996, https://doi.org/10.1016/j.eurpolymj.2023.111996.
- [60] M.A. Hayat (Ed.), Principles and Techniques of Electron Microscopy: Biological Applications, 4th ed, Cambridge University Press, Cambridge, UK; New York, 2000
- [61] E. Choppe, F. Puaud, T. Nicolai, L. Benyahia, Rheology of xanthan solutions as a function of temperature, concentration and ionic strength, Carbohydr. Polym. 82 (2010) 1228–1235, https://doi.org/10.1016/j.carbpol.2010.06.056.
- [62] Y. Matsuda, F. Sugiura, J.W. Mays, S. Tasaka, Atomic force microscopy of thermally renatured xanthan with low molar mass, Polym. J. 47 (2015) 282–285, https://doi.org/10.1038/pj.2014.102.
- [63] S.K. Filippov, R. Khusnutdinov, A. Murmiliuk, W. Inam, L.Ya. Zakharova, H. Zhang, V.V. Khutoryanskiy, Dynamic light scattering and transmission electron microscopy in drug delivery: a roadmap for correct characterization of nanoparticles and interpretation of results, Mater. Horiz. 10 (2023) 5354–5370, https://doi.org/10.1039/D3MH00717K.

- [64] X. Liu, M. Haddou, I. Grillo, Z. Mana, J.-P. Chapel, C. Schatz, Early stage kinetics of polyelectrolyte complex coacervation monitored through stopped-flow light scattering, Soft Matter 12 (2016) 9030–9038, https://doi.org/10.1039/ C6SM019791
- [65] C. Schatz, J.-M. Lucas, C. Viton, A. Domard, C. Pichot, T. Delair, Formation and properties of positively charged colloids based on polyelectrolyte complexes of biopolymers, Langmuir 20 (2004) 7766–7778, https://doi.org/10.1021/ la049460m.
- [66] M. Rubinstein, Q. Liao, S. Panyukov, Structure of liquid coacervates formed by oppositely charged polyelectrolytes, Macromolecules 51 (2018) 9572–9588, https://doi.org/10.1021/acs.macromol.8b02059.
- [67] A. Hugerth, N. Caram-Lelham, L.-O. Sundelöf, The effect of charge density and conformation on the polyelectrolyte complex formation between carrageenan and chitosan, Carbohydr. Polym. 34 (1997) 149–156, https://doi.org/10.1016/S0144-8617(97)00088-X.
- [68] J. Chen, J.A. Heitmann, M.A. Hubbe, Dependency of polyelectrolyte complex stoichiometry on the order of addition. 1. Effect of salt concentration during streaming current titrations with strong poly-acid and poly-base, Colloids Surf. A Physicochem. Eng. Asp. 223 (2003) 215–230, https://doi.org/10.1016/S0927-7757(03)00222.x
- [69] J. Koetz, K.-J. Linow, B. Philipp, L.P. Hu, O. Vogl, Effects of charge density and structure of side-chain branching on the composition of polyanion-polycation complexes, Polymer 27 (1986) 1574–1580, https://doi.org/10.1016/0032-3861 (86)90107-2
- [70] B. Vishalakshi, S. Ghosh, V. Kalpagam, The effects of charge density and concentration on the composition of polyelectrolyte complexes, Polymer 34 (1993) 3270–3275, https://doi.org/10.1016/0032-3861(93)90401-U.
- [71] T. Borodina, A. Gileva, R. Ákasov, D. Trushina, S. Burov, N. Klyachko, Y. González-Alfaro, T. Bukreeva, E. Markvicheva, Fabrication and evaluation of nanocontainers for lipophilic anticancer drug delivery in 3D in vitro model, J. Biomed. Mater. Res. 109 (2021) 527–537, https://doi.org/10.1002/jbm.b.34721.
- [72] X. Liu, H. Gao, F. Huang, X. Pei, Y. An, Z. Zhang, L. Shi, Structure change of mixed shell polymeric micelles and its interaction with bio-targets as probed by the 1anilino-8-naphthalene sulfonate (ANS) fluorescence, Polymer 54 (2013) 3633–3640, https://doi.org/10.1016/j.polymer.2013.05.001.
- [73] K. Akiyoshi, S. Yamaguchi, J. Sunamoto, Self-aggregates of hydrophobic polysaccharide derivatives, Chem. Lett. 20 (1991) 1263–1266, https://doi.org/ 10.1246/cl.1991.1263.
- [74] Y. Chen, S. Jiang, Q. Chen, Q. Liu, B. Kong, Antioxidant activities and emulsifying properties of porcine plasma protein hydrolysates modified by oxidized tannic acid and oxidized chlorogenic acid, Process Biochem. 79 (2019) 105–113, https://doi. org/10.1016/j.procbio.2018.12.026.
- [75] D. Matulis, C.G. Baumann, V.A. Bloomfield, R.E. Lovrien, 1-Anilino-8-naphthalene sulfonate as a protein conformational tightening agent, Biopolymers 49 (1999) 451–458, https://doi.org/10.1002/(SICI)1097-0282(199905)49:6<451::AID-BIP3>3.0.CO:2-6.
- [76] D. Essassi, R. Zini, J.-P. Tillement, Use of 1-Anilino-8-naphthalene sulfonate as a fluorescent probe in the investigation of drug interactions with human alpha-1-acid glycoprotein and serum albumin, J. Pharm. Sci. 79 (1990) 9–13, https://doi.org/ 10.1002/jps.2600790104.
- [77] K.R. Jayappriyan, R. Rajkumar, V. Venkatakrishnan, S. Nagaraj, R. Rengasamy, In vitro anticancer activity of natural β-carotene from Dunaliella salina EU5891199 in PC-3 cells, Biomed. Prev. Nutr. 3 (2013) 99–105, https://doi.org/10.1016/j.bionut.2012.08.003.
- [78] F. Azhar, H. Naureen, G. Shahnaz, S.D.A. Hamdani, M.H. Kiani, S. Khattak, M. K. Manna, M.M. Babar, J. Rajadas, A. Rahdar, A.M. Díez-Pascual, Development of chitosan based β-carotene mucoadhesive formulation for skin cancer treatment, Int. J. Biol. Macromol. 253 (2023) 126659, https://doi.org/10.1016/j.iibiomac.2023.126659
- [79] Y. Wei, C. Sun, L. Dai, X. Zhan, Y. Gao, Structure, physicochemical stability and in vitro simulated gastrointestinal digestion properties of  $\beta$ -carotene loaded zein-

- propylene glycol alginate composite nanoparticles fabricated by emulsification-evaporation method, Food Hydrocoll. 81 (2018) 149–158, https://doi.org/10.1016/j.foodhyd.2018.02.042.
- [80] S.M. Wood, C. Beckham, A. Yosioka, H. Darban, R.R. Watson, β-Carotene and selenium supplementation enhances immune response in aged humans, Integr. Med. 2 (2000) 85–92, https://doi.org/10.1016/S1096-2190(00)00009-3.
- [81] S. Liu, J. Zhang, R. Fu, H. Feng, Y. Chu, D. Huang, H. Liu, C. Li, C. Ma, A.M. Abd El-Aty, Improved stability and aqueous solubility of β-carotene via encapsulation in self-assembled bioactive oleanolic acid nanoparticles, Food Chem. 373 (2022) 131498, https://doi.org/10.1016/j.foodchem.2021.131498.
- [82] D.H. Lee, K.S. Kwon, D. Jeong, I.H. Kim, H.S. Nam, J.-Y. Kim, Structural and physicochemical properties of composites between starch nanoparticles and β-carotene prepared via nanoprecipitation, Int. J. Biol. Macromol. 214 (2022) 100–110, https://doi.org/10.1016/j.ijbiomac.2022.06.062.
- [83] M. Lan, Y. Fu, H. Dai, L. Ma, Y. Yu, H. Zhu, H. Wang, Y. Zhang, Encapsulation of β-carotene by self-assembly of rapeseed meal-derived peptides: Factor optimization and structural characterization, LWT 138 (2021) 110456, https://doi.org/ 10.1016/j.lwr.2020.110456
- [84] J.D. Koch, J. Gronki, R.K. Hanson, Measurements of near-UV absorption spectra of acetone and 3-pentanone at high temperatures, J. Quant. Spectrosc. Radiat. Transf. 109 (2008) 2037–2044, https://doi.org/10.1016/j.jqsrt.2008.02.010.
- [85] N. Barbero, M. Coletti, F. Catalano, S. Visentin, Exploring gold nanoparticles interaction with mucins: a spectroscopic-based study, Int. J. Pharm. 535 (2018) 438–443, https://doi.org/10.1016/j.ijpharm.2017.11.026.
- [86] V.N. Boya, R. Lovett, S. Setua, V. Gandhi, P.K.B. Nagesh, S. Khan, M. Jaggi, M. M. Yallapu, S.C. Chauhan, Probing mucin interaction behavior of magnetic nanoparticles, J. Colloid Interface Sci. 488 (2017) 258–268, https://doi.org/10.1016/j.jcis.2016.10.090.
- [87] P.C. Griffiths, B. Cattoz, M.S. Ibrahim, J.C. Anuonye, Probing the interaction of nanoparticles with mucin for drug delivery applications using dynamic light scattering, Eur. J. Pharm. Biopharm. 97 (2015) 218–222, https://doi.org/10.1016/ j.ejpb.2015.05.004.
- [88] M. Tollemeto, I. Badillo-Ramírez, L.H.E. Thamdrup, Y. Li, M. Ghavami, T.P. Padial, J.B. Christensen, J. Van Hest, A. Boisen, A systematic study on the physicochemical interactions between polymeric micelles and mucin: toward the development of optimal drug delivery nanocarriers, Adv. Mater. Interfaces 11 (2024) 2400107, https://doi.org/10.1002/admi.202400107.
- [89] N.A. Peppas, Y. Huang, Nanoscale technology of mucoadhesive interactions, Adv. Drug Deliv. Rev. 56 (2004) 1675–1687, https://doi.org/10.1016/j. addr.2004.03.001.
- [90] M. Ahmad, C. Ritzoulis, J. Chen, H. Meigui, R. Bushra, Y. Jin, H. Xiao, Xanthan gum – mucin complexation: molecular interactions, thermodynamics, and rheological analysis, Food Hydrocoll. 114 (2021) 106579, https://doi.org/ 10.1016/i.foodhyd.2020.106579.
- [91] G.P. Andrews, T.P. Laverty, D.S. Jones, Mucoadhesive polymeric platforms for controlled drug delivery, Eur. J. Pharm. Biopharm. 71 (2009) 505–518, https:// doi.org/10.1016/j.ejpb.2008.09.028.
- [92] A. Cano-Vicent, A. Tuñón-Molina, H. Bakshi, R. Sabater I Serra, I.M. Alfagih, M. M. Tambuwala, Á. Serrano-Aroca, Biocompatible alginate film crosslinked with Ca<sup>2</sup> and Zn<sup>2+</sup> possesses antibacterial, antiviral, and anticancer activities, ACS Omega 8 (2023) 24396–24405, https://doi.org/10.1021/acsomega.3c01935.
- [93] A. Saarai, V. Kasparkova, T. Sedlacek, P. Saha, On the development and characterisation of crosslinked sodium alginate/gelatine hydrogels, J. Mech. Behav. Biomed. Mater. 18 (2013) 152–166, https://doi.org/10.1016/j. jmbbm.2012.11.010.
- [94] L. Guo, H. Sato, T. Hashimoto, Y. Ozaki, FTIR study on hydrogen-bonding interactions in biodegradable polymer blends of poly(3-hydroxybutyrate) and poly (4-vinylphenol), Macromolecules 43 (2010) 3897–3902, https://doi.org/10.1021/ ma100307m.